LUND UNIVERSITY

Laser-Produced Plasmas for Particle Acceleration

Svensson, Kristoffer

2012

Link to publication

Citation for published version (APA):
Svensson, K. (2012). *Laser-Produced Plasmas for Particle Acceleration*. [Licentiate Thesis, Atomic Physics]. Division of Atomic Physics, Department of Physics, Faculty of Engineering, LTH, Lund University.

Total number of authors:
1

General rights
Unless other specific re-use rights are stated the following general rights apply:
Copyright and moral rights for the publications made accessible in the public portal are retained by the authors and/or other copyright owners and it is a condition of accessing publications that users recognise and abide by the legal requirements associated with these rights.
• Users may download and print one copy of any publication from the public portal for the purpose of private study or research.
• You may not further distribute the material or use it for any profit-making activity or commercial gain
• You may freely distribute the URL identifying the publication in the public portal

Read more about Creative commons licenses: https://creativecommons.org/licenses/

Take down policy
If you believe that this document breaches copyright please contact us providing details, and we will remove access to the work immediately and investigate your claim.

LUND UNIVERSITY

PO Box 117
221 00 Lund
+46 46-222 00 00

Laser-Produced Plasmas for Particle Acceleration

Kristoffer Svensson

Licentiate Thesis
2012

Lund University

Laser-Produced Plasmas for Particle Acceleration

© 2012 Kristoffer Svensson
All rights reserved
Printed in Sweden by Media-Tryck, Lund, 2012

Division of Atomic Physics
Department of Physics
Faculty of Engineering, LTH
Lund University
P.O. Box 118
SE–221 00 Lund
Sweden

http://www.atomic.physics.lu.se

ISSN 0281-2762
Lund Reports on Atomic Physics, LRAP-456

ISBN 978-91-7473-321-1

To Elisabeth. You are the sunshine in my life.

Abstract

This thesis describes experimental studies that aim to stabilise and optimise laser-based particle accelerators. The technique is called laser wakefield acceleration, where electric fields of the order of 10^2 GV/m accelerate electrons to high energies ($\sim 10^2$ MeV) over mm-distances in laser-produced plasmas.

Among the prerequisites for this acceleration technique to produce electron beams are laser intensities higher than 10^{18} W/cm^2 and sub-ps laser-pulse durations, both of which have seen rapid development since the invention of chirped pulse amplification. The laser is focused in a gas, which instantly ionises. In the created plasma, the propagating laser pulse creates a wave, which can accelerate injected electrons. Under the right experimental conditions, the injection mechanism is automatic, and is called self-injection. The conditions required for self-injection to occur are experimentally explored and presented in the thesis. In addition to the accelerated electrons, collimated beams of x-rays, called betatron radiation, are produced during the interaction.

The thesis also discusses several ways to enhance important parameters, such as relative energy spread and divergence, of the resulting particle beams, which is important for future applications. By using smart target designs, it is possible to reduce both the spectral and spatial spread of laser wakefield accelerated electrons. In the experiment where density-downramp injection was implemented, relative energy spreads as low as 1 % were achieved. During the experiment when the target consisted of a gas-filled capillary, the x-ray fluence was increased by a factor of ten when compared to betatron radiation generated in a supersonic gas jet. It is also shown in the thesis that the choice of gas is important, and increased stability is achieved if hydrogen is used as target gas instead of helium.

List of Publications

The following papers form the scientific basis on which this Licentiate thesis is founded. In the text, the papers will be referred to by their respective Roman numeral.

I **Influence of Gas Media on Electron Beam Quality**
K. Svensson, F. Wojda, M. Burza, G. Genoud, A. Persson, L. Senje, O. Lundh, and C.-G. Wahlström.
Manuscript in preparation.

II **Staged Laser Wakefield Acceleration Using Double Density Ramps**
M. Burza, A. Gonoskov, K. Svensson, F. Wojda, A. Persson, M. Hansson, G. Genoud, M. Marklund, C.-G. Wahlström, and O. Lundh.
Manuscript in preparation.

III **Enhancement of X-Rays Generated by a Guided Laser Wakefield Accelerator inside Capillary Tubes**
J. Ju, K. Svensson, A. Döpp, H. E. Ferrari, K. Cassou, O. Neveu, G. Genoud, F. Wojda, M. Burza, A. Persson, O. Lundh, C.-G. Wahlström, and B. Cros.
Accepted for publication in Appl. Phys. Lett.

IV **Self-Injection Threshold in Self-Guided Laser Wakefield Accelerators**
S. P. D. Mangles, G. Genoud, M. S. Bloom, M. Burza, Z. Najmudin, A. Persson, K. Svensson, A. G. R. Thomas and C.-G. Wahlström.
Phys. Rev. ST Accel. Beams **15**, 011302 (2012).

Additional paper by the author:

Hollow Microspheres as Targets for Staged Laser-Driven Proton Acceleration

M. Burza, A. Gonoskov, G. Genoud, A. Persson, K. Svensson, M. Quinn, P. McKenna, M. Marklund, and C.-G. Wahlström. *New J. Phys.* **13**, 013030 (2011).

Contents

1 Introduction **1**

2 Scientific Background **3**
2.1 Gaussian Laser Beams . . . 3
2.2 Ionisation . . . 5
2.3 Laser-Plasma Interaction . . . 5
2.3.1 Linear Regime . . . 5
2.3.2 Non-Linear Regime . . . 7
2.3.3 Quasi-Mononergetic Electron Beams . . . 7
2.3.4 X-Ray Generation . . . 8
2.3.5 Relativistic Effects . . . 8
2.3.6 Relativistic Self-Focusing . . . 8
2.3.7 Laser Pulse Compression . . . 9
2.3.8 Pump Depletion . . . 9

3 Experimental Methods **11**
3.1 Laser System & Target Chamber . . . 11
3.1.1 Gas Targets . . . 14
Gas Jet . . . 14
Dielectric Capillary Tubes . . . 15
3.2 Diagnostics . . . 16
3.2.1 Electron Detection . . . 16
Electron Spectrometer . . . 16
3.2.2 Interferometer . . . 21
3.2.3 X-Ray Detection . . . 23

4 Summary of Experimental Results **25**
4.1 Influence of Gas Media on Electron Beam Quality in Laser Wakefield Accelerators . . . 25
4.1.1 Experiment . . . 25
4.1.2 Results . . . 26
4.2 Staged Laser Wakefield Acceleration Using Double Density Ramps . . . 29
4.2.1 Experiment . . . 29
4.2.2 Results . . . 30
4.3 Enhancement of X-Rays Generated by a Guided Laser Wakefield Accelerator inside Capillary Tubes . . . 32
4.3.1 Experiment . . . 32
4.3.2 Results . . . 32
4.4 Self-Injection Threshold in Self-Guided Laser Wakefield Accelerators . . . 34
4.4.1 Experiment . . . 34
4.4.2 Results . . . 34

5 Summary & Outlook **37**

Role of the Author **39**

Acknowledgments **41**

References **43**

Papers

I	Influence of Gas Media on Electron Beam Quality	49
II	Staged Laser Wakefield Acceleration Using Double Density Ramps	55
III	Enhancement of X-Rays Generated by a Guided Laser Wakefield Accelerator inside Capillary Tubes	61
IV	Self-Injection Threshold in Self-Guided Laser Wakefield Accelerators	67

Chapter 1

Introduction

In 1979, T. Tajima and J. M. Dawson proposed a new scheme to accelerate electrons in laser-produced plasmas [1], which is now called laser wakefield acceleration. They predicted that electrons could be accelerated to gigaelectronvolt energies over only a few centimetres. This length-scale should be compared to conventional accelerators, where the acceleration length needs to be roughly a thousand times longer, because they are limited by electrical breakdown. This means that the maximum electrical field is $\sim 10^2\,\mathrm{MV/m}$, while the field strength of a plasma accelerator is of the order of $\sim 10^2\,\mathrm{GV/m}$. However, it was not possible to reach the laser intensities needed until the invention of chirped pulse amplification [2] in the late 1980s.

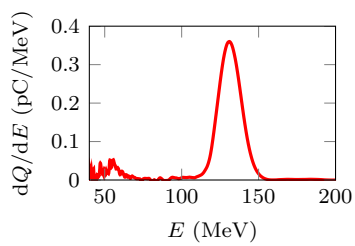

Figure 1.1. *An electron energy spectrum with a quasi-monoenergetic peak at $E = 130$ MeV. The total charge of the spectrum is $Q = 7$ pC.*

To accelerate electrons in laser-produced plasmas, a very short ($< 10^2$ fs) and very intense ($\sim 10^{18}\,\mathrm{W/cm^2}$) laser pulse is focused into a gas, which is instantly ionised. As the laser propagates through the plasma, it displaces electrons by the ponderomotive force, and a plasma wave is created when the displaced electrons start to oscillate due to space charge. The charge separation will also induce large transverse and longitudinal electric fields. Under the right conditions, electrons can be injected to the accelerating phase of the plasma wave, where the large electrical field can accelerate the electrons to high energies ($\sim$GeV). If the driving laser pulse is intense enough, the injection of electrons can happen automatically. This process is called self-injection, which was experimentally observed in the mid-1990s [3], and the threshold for it to occur is explored in Paper **IV**. In the first experiments, the electron energy spectra were broad. However, in 2004 a breakthrough occurred when three independent research teams observed quasi-monoenergetic energy spectra, such as the one displayed in Fig. 1.1, for laser wakefield accelerated electrons [4–6]. It is also possible to reduce the energy spread by utilising controlled injection techniques, such as ionisation injection [7, 8],

colliding pulse injection [9] or density-downramp injection [10], the last of which is implemented in Paper **II**.

Since the intensity of the laser pulse is very high, there are many nonlinear effects that affect the pulse evolution. Some are favourable, such as relativistic self-focusing which counteracts diffraction, while others might have negative effects on the resulting electron beams. In Paper **I** we study the stability of important electron beam parameters, and which effect the choice of gas has.

As the electrons are accelerated by the longitudinal fields inside the plasma wave, the transversal fields will focus the electron beam. However, it will also cause the electrons to oscillate, or wiggle, about the optical axis. This wiggle motion will cause the electrons to emit short-wavelength radiation, and the resulting x-rays are called betatron radiation. Thus, laser wakefield accelerators are also a promising technique for compact x-ray sources, and in Paper **III** we report on ways to increase the x-ray fluence by altering the target.

Chapter 2

Scientific Background

In this part of the thesis, Some of the basic theory behind electron acceleration in laser-produced plasmas is explained and important expressions used in the following chapters and in the papers are introduced.

2.1 Gaussian Laser Beams

Mathematically, laser beams are often represented by plane waves. However, this is an idealisation of the physical reality, since a plane wave exists over all space. Therefore, describing a wave confined in space is done by a complex Gaussian function, $\mathbf{E}(t, \rho, z)$. Here, t is time, ρ is the radial distance from the optical axis and z is the distance along the propagation axis from the beam waist. It is also assumed that the laser is linearly polarised, so $\mathbf{E}/E = \hat{\mathbf{e}}_x$ and the beam is propagating along z. In the experiments presented in this thesis, the laser is compressed to ultra-short pulses, which means that the Gaussian function describing the laser also must be confined in time. This is done by multiplying $\mathbf{E}$ with

$$\Gamma(t, z) = \exp\left[-2\ln 2\left(\frac{t - z/c}{\tau}\right)^2\right], \tag{2.1}$$

which is also a Gaussian function with the full width at half maximum time spread τ.[1]

When focusing a Gaussian beam, the focal spot radius[2] is given by

$$w_0 = \frac{2\lambda_0}{\pi} f/\#, \tag{2.2}$$

where $f/\#$ is the focal length divided by the beam diameter and λ_0 is the central wavelength of the pulse. The beam radius at

[1] *There are several ways to define the duration of a laser pulse, and in this section, the full width at half maximum, τ_{FWHM}, is used. For convenience, it will simply be denoted by τ.*

[2] *As for the time duration of the pulse, it's radius can be defined in several ways. In this section, it is defined to be the radius where the intensity has decreased by a factor e^2.*

Numerical example. *The peak intensity for a laser pulse with $E_{pulse} = 1$ J, $\tau = 42$ fs and $w_0 = 8$ μm is 16×10^{18} W/cm^2.*

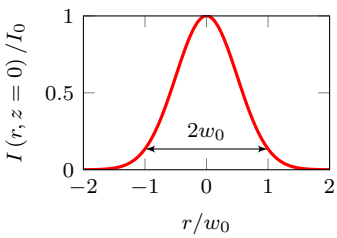

Figure 2.2. *The intensity distribution of a Gaussian beam at the plane of the beam waist. The spot size, $2w_0$, is the transversal length where the intensity has decreased by a factor e^2.*

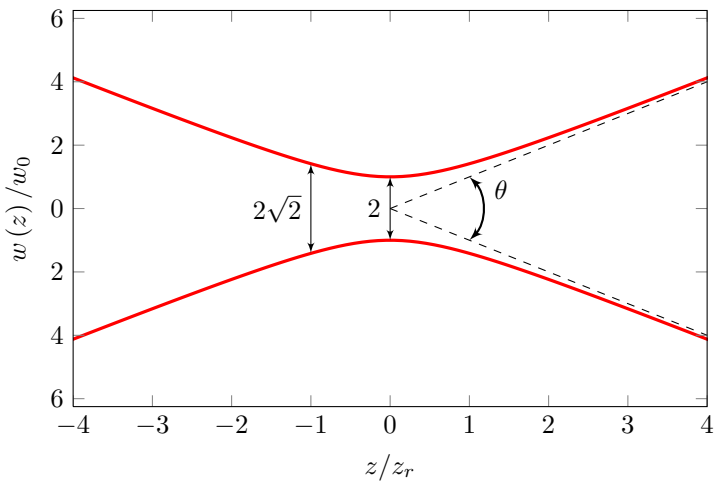

Figure 2.1. *The waist of a focused Gaussian laser beam. The minimum diameter is $2w_0$ which has increased to $2\sqrt{2}w_0$ after one Rayleigh length. The far-field ($z \gg z_r$) divergence of the beam is θ.*

some position z can then be calculated by

$$w(z) = w_0 \sqrt{1 + \left(\frac{z}{z_r}\right)^2} \tag{2.3}$$

and is displayed in Fig. 2.1. In Eq. 2.3, z_r is the Rayleigh length, which is defined as the distance it takes for the beam's cross-sectional area to increase by a factor of two.

Knowing the focal spot size of the laser beam, it is possible to determine the intensity distribution as

$$I(t, \rho, z) = I_0 \left(\frac{w_0}{w(z)}\right)^2 \exp\left[-\frac{2\rho^2}{w^2(z)}\right] \Gamma^2(t, z). \tag{2.4}$$

The intensity distribution at the beam waist is shown in Fig. 2.2. The peak intensity, I_0, is given by

$$I_0 = \sqrt{\frac{16 \ln 2}{\pi}} \times \frac{E_{\text{pulse}}}{\pi w_0^2 \tau}, \tag{2.5}$$

where E_{pulse} is the pulse energy.

Light can also be described by it's vector and scalar potentials, $\mathbf{A}$ and ϕ respectively, where $\mathbf{B} = \nabla \times \mathbf{A}$ and $\mathbf{E} = -\nabla\phi - \frac{\partial \mathbf{A}}{\partial t}$. A useful definition is the normalised vector potential,

$$\mathbf{a} = \frac{e\mathbf{A}}{m_e c}, \tag{2.6}$$

where e is the elementary charge and m_e is the electron mass. The maximum amplitude of Eq. 2.6 is often used to characterise

the strength of the laser pulse, and can be calculated as

$$a_0 \approx 0.86\lambda_0\,[\mu\mathrm{m}]\sqrt{I_0\left[\mathrm{W/cm^2}\right]}, \tag{2.7}$$

by noting that $\mathbf{A} = A_0 \cos(kz - \omega_0 t)\,\hat{\mathbf{e}}_x$ and $I = c\epsilon_0 |\mathbf{E}|^2/2$. Here, ω_0 is angular laser frequency, $k = 2\pi/\lambda_0$ and ϵ_0 is the permittivity of free space.

In the experiments discussed in this thesis, and reported in Papers **I** to **IV**, we were working at intensities corresponding to $a_0 > 1$. When $a_0 \gtrsim 1$, electrons in the laser field will oscillate with a speed $v_\perp \approx c$, which means that relativistic effects must be taken into account for an accurate description of the physics.

Table 2.1. *The required intensities according to Eq. 2.8 for ionising atoms relevant to this thesis*

Ion	Intensity ($\mathrm{W/cm^2}$)
H^+	1.4×10^{14}
He^+	1.4×10^{15}
He^{2+}	8.8×10^{15}

2.2 Ionisation

The electric field in a laser pulse with an intensity $\sim 10^{18}\,\mathrm{W/cm^2}$ is so strong that it will drastically perturb the Coulomb potential felt by the electrons in an atom, and electrons will be able to spontaneously escape due to over-the-barrier-ionisation. The critical field needed to perturb the potential to this point is given by $E_c = E_{\mathrm{ion}}^2/4Ze^3$, which yields an effective ionisation intensity of [11]

$$I_{\mathrm{ionisation}}\left[\mathrm{W/cm^2}\right] \approx 4 \times 10^9\,(E_{\mathrm{ion}}\,[\mathrm{eV}])^4\,Z^{-2}, \tag{2.8}$$

where E_{ion} is the ionisation energy and Z is the charge state of the resulting ion. Comparing the required intensities in Table 2.1 with the typical intensity achieved by our laser system (see Section 3.1), it is realised that only the front of the laser pulse has to reach the medium for it to ionise. Thus, the main laser pulse is interacting with a fully ionised plasma.

2.3 Laser-Plasma Interaction

In this section, we highlight the importance to distinguish between different regimes of laser-plasma interaction; one where the pump strength is low enough so that relativistic effects can be ignored, and the other where relativistic effects are utterly important.

2.3.1 Linear Regime

A plasma can be modelled as a fluid consisting of free electrons and ions. However, during the time-scale of a ultra-short laser pulse with $I_0 \approx 10^{19}\,\mathrm{W/cm^2}$, only electrons will move. Since the ions have a much larger mass than electrons, they can be treated as a stationary, positively charged background. The motion of an electron in external electric and magnetic fields is described by the

Numerical example. *Assuming a laser wavelength of 800 nm, the critical density, n_c, for neutral helium at $T = 300$ K is equivalent to a static pressure of 36 bar.*

Lorentz equation, and when the time duration of the laser pulse is very short, the result is a time-averaged force called the ponderomotive force, $\mathbf{F}_p$. The important characteristic is that $\mathbf{F}_p \propto -\nabla I$ [11], which means that the electrons are pushed away from regions of high intensity. The resulting charge separation creates electrostatic fields, and behind the laser pulse, displaced electrons will start to oscillate. It is possible to derive a wave equation, which describes the collective motion of these electrons in the plasma. For a small charge density displacement Δn_e, it's solution yields a dispersion relation for propagation of an electromagnetic wave (laser pulse) with frequency ω_0 in the plasma as

$$\omega_0^2 - \frac{e^2 n_e}{\epsilon_0 m_e} = \omega_0^2 - \omega_p^2 = k^2 c^2, \tag{2.9}$$

where ω_p is the plasma frequency. It is also possible to determine a corresponding refractive index, η, of the plasma as $\omega_0/k = c/\eta$, where

$$\eta = \sqrt{1 - \frac{\omega_p^2}{\omega_0^2}}. \tag{2.10}$$

From Eq. 2.9 it is possible to define two different types of plasmas. The first is $\omega_0 < \omega_p$, for which k becomes imaginary. In this case, called an overdense plasma, the electrons are able to move together with the electric field in the laser pulse, which means that the laser field is effectively stopped and the pulse can not propagate through the plasma. The second case is when $\omega_0 > \omega_p$, and the plasma is transparent for the incoming laser pulse. This is called an underdense plasma. It is possible to determine a critical density, n_c, when the laser frequency is equal to the plasma frequency, which marks the boundary between these plasma types, and it becomes

$$n_c = \frac{\epsilon_0 m_e \omega_0^2}{e^2}. \tag{2.11}$$

Overdense plasmas are often formed when an intense laser pulse interacts with a solid target. They can be used for ion acceleration, and one technique is called target normal sheath acceleration [12–14]. However, this subject is not covered in this thesis and from now on only underdense plasmas, where laser propagation is allowed, will be considered.

From Eq. 2.9 it is possible to determine a plasma wavelength as

$$\lambda_p = \frac{2\pi v_p}{\omega_p} = \frac{2\pi\beta c}{\omega_p}, \tag{2.12}$$

where $\beta = v_p/c$ is the speed of the plasma wave normalised to the speed of light. It is therefore possible to resonantly drive the plasma wave by matching the length of the laser pulse to the plasma wavelength. Assuming a Gaussian pulse, and a small

relative electron density perturbation the resonance condition is [11]

$$c\tau = \frac{\sqrt{2\ln 2}}{\pi}\lambda_p \approx 0.4\lambda_p. \tag{2.13}$$

This resonance condition is also valid for large charge separations, but then the plasma wavelength must be changed to the relativistic counterpart, which will be described in Section 2.3.5.

From Eq. 2.9, it is also possible to find the phase velocity of the plasma wave, which equals the group velocity of the laser pulse, as

$$v_p = \frac{\partial\omega_0}{\partial k} = \frac{kc^2}{\sqrt{k^2c^2+\omega_p^2}}. \tag{2.14}$$

2.3.2 Non-Linear Regime

When the intensity of the laser pulse becomes very high (corresponding to $a_0 > 1$), the speed of the displaced electrons will start to approach the phase velocity, v_p, of the plasma wave. The result is that the wave breaks and it's growth is effectively stopped. It is also possible for electrons to enter the accelerating phase behind the laser pulse, and be accelerated by the extremely high electric fields generated by the charge separation. This way of letting electrons enter the accelerating region of the plasma wave is called self-injection. It is also the process which is discussed in Papers **I** and **III**, and the threshold for it to occur is explored in Paper **IV**.

As the electrons are accelerated, they will start to catch up with the laser pulse, and as they outrun the plasma wave, they will start to decelerate. This is called dephasing,[3] and will happen after an acceleration length of [15]

$$L_\mathrm{d} = \frac{4c\omega_0^2}{3\omega_p^3}\sqrt{a_0}. \tag{2.15}$$

If all electrons are expelled behind the laser pulse, the result is a positively charged ion channel. This is called the blow-out regime.

2.3.3 Quasi-Mononergetic Electron Beams

If electrons are continuously injected into the plasma wave behind the laser pulse, the resulting electron spectrum will have a large energy spread. However, if the injection can be made very local, all electrons in the bunch will feel the same acceleration force over the same distance, and thus reach the same energy after acceleration. To achieve this, the wavebreaking must be local and during only a very short time. It has been shown that operating just

[3] *Dephasing can also occur in the linear regime. In this case the dephasing length is given by [15]* $L_\mathrm{d} = \lambda_p\omega_0^2/2\pi\omega_p^2$.

above the injection threshold density, which is the lowest density where electrons are injected, the injection mechanism obtains these crucial properties. The effect arises due to beam loading [16], which means that the electric field of the injected electrons shields the accelerating field and stops any further injection.

2.3.4 X-Ray Generation

Inside the plasma wave where the electrons are accelerated, strong radial focusing forces exist due to the positively charged background of the stationary ions. Thus, if an electron is injected off-axis, it will gain transverse momentum and oscillate about the optical axis. As for all charged particles, acceleration will cause the particle to emit radiation. The x-rays emitted are called betatron radiation, and due to the relativistic velocity of the electrons in the forward directions, these x-rays form a collimated beam also in the forward direction. It has been shown that the spectrum is synchrotron-like [17, 18] with keV critical energy.

2.3.5 Relativistic Effects

In some of the expressions in the previous section, the relativistic nature of the electron oscillation has been neglected, thus not being completely accurate for large pump strengths (corresponding to $a_0 > 1$). In this case, the speed of the electron oscillation will start to approach the speed of light, which means that the particles will experience an increase in mass. This will alter the dispersion relation by the transverse relativistic factor $\gamma_\perp = \sqrt{1 + a^2(\rho)/2}$, where $a(\rho) = a_0 \exp\left[-\rho^2/2w_0\right]$ is the laser strength parameter a distance ρ from the axis in the radial direction. Equation 2.9 now becomes

$$\omega_0^2 - \frac{\omega_p^2}{\gamma_\perp} = k^2 c^2. \tag{2.16}$$

This means that the plasma wavelength in the relativistic case becomes

$$\lambda_p^{(r)} = \lambda_p \sqrt{\gamma_\perp}. \tag{2.17}$$

2.3.6 Relativistic Self-Focusing

In an underdense plasma, the electron density is often much lower than the critical density defined in Eq. 2.11. If $n_e \ll n_c$, then also $\omega_p^2 \ll \omega_0^2$ holds. In the relativistic case, the plasma frequency is $\omega_p/\sqrt{\gamma_\perp}$, which means that the refractive index of the plasma can be written as

$$\eta(\rho) - 1 \approx -\frac{n_e}{2n_c}\left(1 - \frac{a^2(\rho)}{4}\right), \tag{2.18}$$

since $a(\rho)$ has a Gaussian shape, η will be peaked at the center of the beam and fall off towards the wings of the pulse. This means that the plasma acts as a positive lens and focuses the beam, counteracting diffraction over several Rayleigh lengths. The power threshold for this type of relativistic self-focusing to occur is given by [19, 20]

$$P_c = \frac{8\pi\epsilon_0 m_e^2 c^5 n_c}{e^2 n_e}. \tag{2.19}$$

2.3.7 Laser Pulse Compression

There is also a longitudinal difference in the refractive index of the plasma. The front of the laser pulse is propagating through a higher refractive index than the back of the pulse, which in the blow out regime propagates in vacuum. This means that the pulse will be compressed in time. A simple estimate of this compression, after a length l, is [21]

$$\tau_f(l) = \tau_0 - \frac{n_e l}{2cn_c}, \tag{2.20}$$

where τ_0 is the initial pulse length.

2.3.8 Pump Depletion

The laser pulse energy is not a constant as it propagates through the medium, since the ionisation and plasma wave excitation requires energy. This means that after a certain length, L_{pd}, all energy in the laser pulse will be depleted. The length is called the pump-depletion length[4] and is given by [15]

$$L_{\mathrm{pd}} = \frac{c\tau_0\omega_0^2}{\omega_p^2} = \frac{c\tau n_c}{n_e}. \tag{2.21}$$

Obviously, the pump-depletion length is shorter for higher electron densities, since more energy is needed to both ionise and displace more electrons. If the acceleration length is limited by pump depletion, then the final pulse length will, according to Eq. 2.20, become $\tau_f\,(l = L_{\mathrm{pd}}) = \tau_0/2$.

[4] *In the linear case, the pump depletion length is given by [15]* $L_{\mathrm{pd}} = \omega_0^2 c\tau/\omega_p^2 a_0^2$.

Chapter 3

Experimental Methods

In this chapter, the Lund multi-terawatt laser system and the experimental vacuum chamber will be presented. At the end, some of the most important diagnostics used during experiments are briefly explained. In all experiments presented in this thesis, an intense and stable laser beam with a focal spot near the diffraction limit was necessary.

3.1 Laser System & Target Chamber

The multi-terawatt laser system at the Lund High-Power Laser Facility, displayed in Fig. 3.1, has as lasing medium a sapphire crystal doped with titanium [22], and generates short high-intensity laser pulses by utilising chirped pulse amplification (CPA) [2]. The Kerr-lens mode-locked oscillator [23], marked with *a* in Fig. 3.2, emits pulses at 80 MHz rate. The light has a central wavelength at 800 nm and a bandwidth of approximately 50 nm. The pulse train exits the oscillator through an output coupler and enters a Pockels cell, which, together with a polariser, selects only ten pulses per second. A Dazzler is in the beam path which

Table 3.1. *Lund multi-terawatt laser parameters*

Central wavelength	800 nm
Pulse energy	1 J
Pulse length	35 fs
Repetition rate	10 Hz
Beam diameter	5 cm
Contrast ratio	$>10^8$
Peak power	30 TW

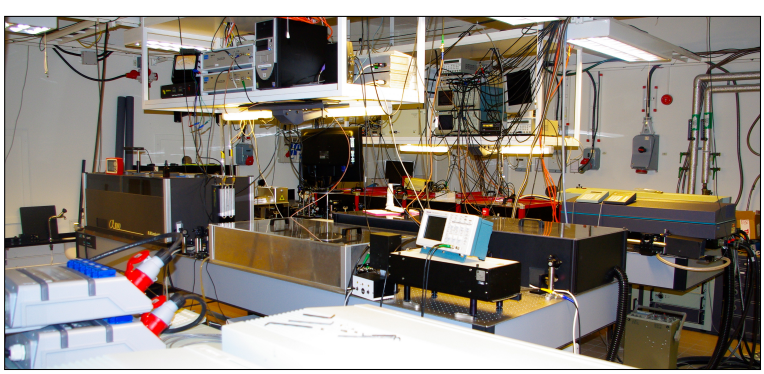

Figure 3.1. *The multi-terawatt laser at the Lund High-Power Laser Facility.*

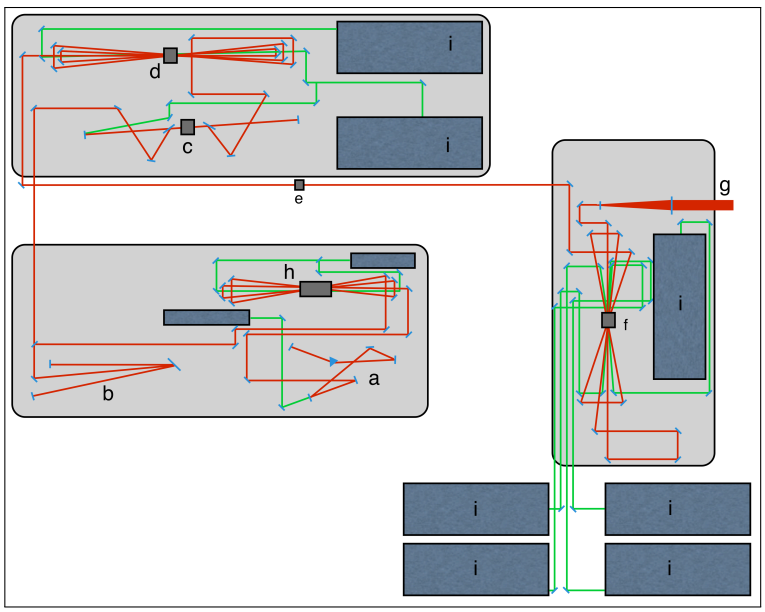

Figure 3.2. *A schematic view of Lund multi-terawatt laser. The main laser beam is coloured red, and pump lasers green. The labelled areas are: (a) oscillator, (b) stretcher, (c) regenerative amplifier, (d) first multi-pass, (e) spatial filter, (f) second multi-pass, (g) output to compressor, (h) preamplifier, and (i) frequency-doubled Nd:YAG lasers pumping the amplifier crystals. Note that the pulse compressor and deformable mirror is not present in the figure.*

shapes the light spectrally to precompensate for gain-narrowing [24] and higher-order dispersion which might occur later in the optical system.

The first part of the CPA-setup, the stretcher, will immediately after the Dazzler increase the pulse length to hundreds of picoseconds, by introducing path length differences between different spectral components of the pulse. There are several ways to introduce this spectral and temporal broadening, and in this setup it is done by a diffraction grating. The long pulse length is needed when amplifying to high pulse energies, otherwise the gain media in the amplifiers and other optical components in the setup will be damaged by non-linear effects, such as self-focusing [25, 26].

The total amplification consists of three different stages; first a regenerative [27] and then two separate multi-pass amplifiers [28]. The last amplifying crystal is cryogenically cooled. In the first stage, the laser pulses make 15 round-trips through the closed cavity before being switched out to the first multi-pass. After five passes in the second stage, the pulse energy reaches 100 mJ. In preparation for the third, and last, amplifier, a spatial filter cleans the beam from high-frequency noise, otherwise it might be in-homogenous and prevent an effective pulse compression or even damage the compressor gratings. The actual compression, which brings the pulse duration down to 35 fs, takes place under vacuum, since the pulses otherwise are destroyed by non-linear effects in air. As stated earlier, the pulses are optimised by both the Dazzler and a spatial filter, but there are also other polarisers

and Pockels cells which, by time-gating, removes pre-pulses and amplified spontaneous emission. The amplification of spontaneous emission for high-power lasers are inevitable. In a hard-pumped, closed cavity, the gain medium will spontaneously emit radiation. If this light starts to make round-trips in the cavity, it will be amplified. After amplification and compression, there is 1 J in each laser pulse and the beam diameter is 5 cm. A schematic overview of the laser system is found in Fig. 3.2 and important experimental laser parameters are summarised in Table 3.1.

The quality of the focal spot is important, as we investigated in Paper **IV** (briefly summarised in Section 4.4). One way to optimise the focus of a laser beam is to use an adaptive optics system to alter the wavefront of the light to reduce optical aberrations. Our system consists of a deformable mirror and a wavefront sensitive detector (Phasics SID 4). The mirror itself has a reflectivity higher than 99.9 % for 800 nm wavelengths and can deform its surface by applying high voltages over 32 different control electrodes, due to the inverse piezo-electric effect. One of the 32 electrodes changes the curvature of the mirror, which makes it possible to fine-tune the position of the focal plane inside the experimental target chamber. One of the key elements of Paper **IV** was the deformable mirror's ability to add spherical aberration, which alters the energy within the full with at half maximum of the focal spot.

Two different focusing optics, both off-axis parabolic mirrors, have been used during the experimental work. In Papers **I** to **III**, an $f/15$ was used, and in **IV** an $f/9$. The f-number of the optic determines the focused beam size. The resulting FWHM spot sizes for the mirrors in all papers are collected in Table 3.2.

Since the intensity of the light during experiments is very high, all experiments have to take place under vacuum. The chamber we use is an aluminium cylinder with 60 cm radius and a picture of it can be seen in Fig. 3.3. Underneath the chamber floor, an extra compartment is attached which houses three orthogonal translation stages. The translation stages gives us the ability to move the gas jet position i three dimensions under vacuum. A number of ports on top and on the side of the chamber enables us to mount external diagnostics (see Section 3.2) or connect other equipment. An example is the motorised mirrors, which are part of the laser alignment system. To power and control them, cables are connected by feed-throughs that do not break the vacuum. We have a wide range of flanges, pipes and cubes that connect to the ports, which makes this a versatile vacuum chamber that can adapt to very different types of experiments.

A typical experimental setup is shown in Fig. 3.4. Note that there are usually more equipment in the setup, but it is left out for viewing purposes. As the beam enters the chamber from the top, it is guided by mirrors onto the off-axis parabola, which focuses

Table 3.2. *The different focal lengths, f, of parabolas used in the papers and the diffraction-limited FWHM spot sizes they can produce*

f	Spot Size	Paper(s)
45 cm	9.6 µm	**IV**
75 cm	16 µm	**I**, **II**, **III**

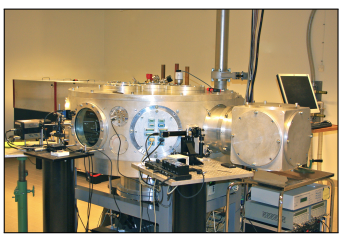

Figure 3.3. *The experimental vacuum chamber with an extra cube containing an off-axis parabolic mirror.*

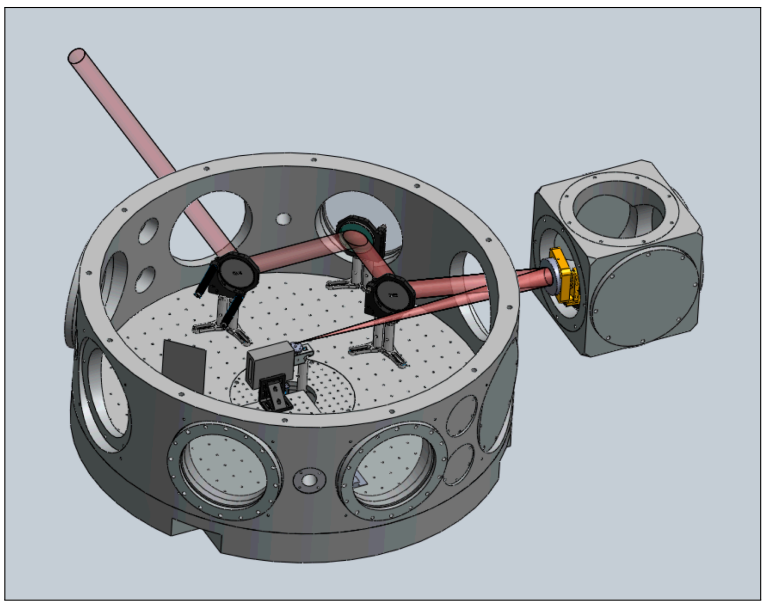

Figure 3.4. *Typical experimental setup for electron acceleration. In the figure, the off-axis parabolic mirror focuses the incoming laser beams towards the gas jet. Directly afterwards, a permanent dipole magnet is mounted on a transversal slide which allows it to move out of the optical axis. A scintillating screen is also visible after the magnet. Note that parts belonging to the alignment system of the laser, the top-view camera, interferometer, the 16-bit CCD camera, as well as the X-ray sensitive CCD camera are not visible in this figure.*

it to a spot size according to Table 3.2.

3.1.1 Gas Targets

During the experimental work, two different types of gas targets have been employed. In the experiments presented in Papers **I**, **II** and **IV** we used a gas jet capable of producing super-sonic flows, and for Paper **III** a glass capillary tube filled with gas served as target.

Gas Jet

The gas jet we use during experiments has a fast opening time, and is opened a few milliseconds before the laser pulse arrives. This is done to ensure a stable gas flow. The nozzle has a conic shape, and is detachable, which makes it possible to adjust the plasma length. During the experimental work described later in this thesis, nozzle diameters of 2 mm and 3 mm were used. To have an efficient plasma wave production, the laser propagation depends on relativistic self-focusing, which is described in Section 2.3.6. Experimentally, a density threshold for self-injection is observed, which puts a lower limit on n_e where injection stops and no electrons are accelerated.

The gas jet is connected to a gas-handling system, which is built by 6 mm steel pipes outside the vacuum chamber (see Fig. 3.5 for a schematic drawing). The system was built to have the ability to mix gases, which is why a gas reservoir is present. However, electron acceleration in gas mixtures is not covered in this thesis.

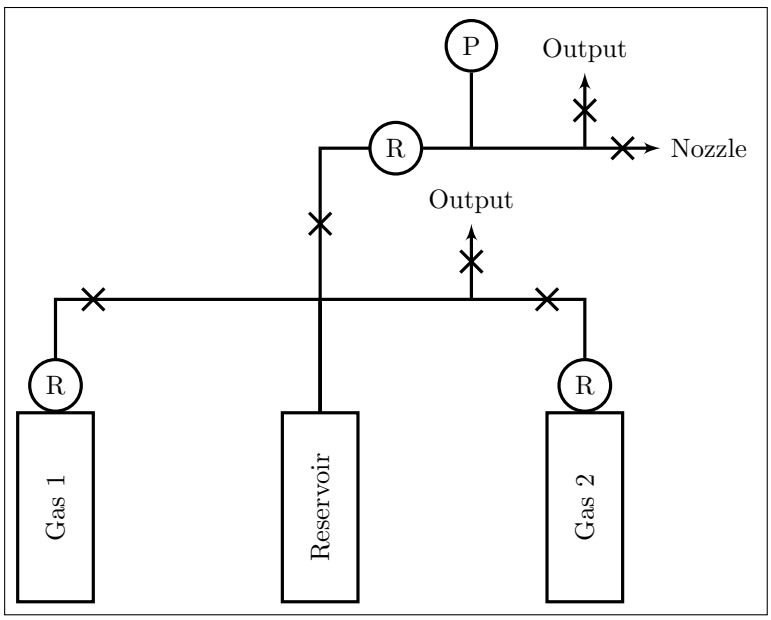

Figure 3.5. *Schematic drawing of the gas handling system outside of the vacuum chamber. The system is capable of mixing gases in a reservoir. In the figure, R denotes regulators, P pressure gauge, and crosses are valves. Two additional outputs enable the system to be partially or completely evacuated.*

The pressure inside the gas lines, which is measured by a pressure gauge (denoted P in Fig. 3.5) determines the resulting electron density, n_e, of the plasma.

Great care is taken to ensure that the focal plane lies close to the edge of the super-sonic gas-flow, since effects such as ionisation defocusing would otherwise prevent the laser from reaching intensities required for laser wakefield acceleration. Thus, a sharp gas jet edge is required, which is why the gas flow has to be supersonic.

Typically, the diffraction length of a focused laser is taken to be the Rayleigh length, z_r in Eq. 2.3. z_r would be the acceleration length limit without relativistic self-focusing (see Section 2.3.6), which counteracts diffraction. The result is that the acceleration is usually limited by either dephasing or pump depletion, which are described in Sections 2.3.2 and 2.3.8, respectively.

Dielectric Capillary Tubes

One way to increase the acceleration length is to use gas-filled dielectric capillary tubes, which act as waveguides for the laser pulse. In addition to guiding the pulse, the capillary will also couple the laser energy outside of the pulse FWHM to the interaction, which is shown in Paper **IV** to not be the case for a gas jet operating in the self-injection regime. Through nonlinear pulse evolution, the intensity of the laser pulse will increase even further as it propagates through the capillary, which makes it possible to

use lower intensities to accelerate electrons than for gas jets utilising self-injection [29]. It has been shown previously in our lab, that plasma waves can be excited and driven by focusing laser pulses into a capillary with lengths up to 8 cm [30], which makes these tubes good candidates for a future increase of acceleration length.

3.2 Diagnostics

The laser-plasma interaction that occurs when the laser beam strikes the gas flow gives rise to interesting physical phenomena described in Section 2.3, which have to be detected. This section discusses three diagnostics, which were important for Papers **I** to **IV**, namely how the electron beam is detected, how the betatron radiation is measured, and how the plasma density is estimated.

3.2.1 Electron Detection

This is, of course, the main diagnostic for electron acceleration experiments and a very important part of Papers **I** to **IV**. The setup we have used in all laser wakefield acceleration investigations consisted of three independent parts; a permanent dipole magnet, a scintillating screen and a CCD camera.

The scintillating screen in the setup detects the electron beam by fluorescent light, and the type we usually use is Kodak Lanex Regular. The residual laser light is stopped by attaching an aluminium plate to the front of the scintillator. To collect the light generated in the Lanex screen, a CCD camera is used, which in Papers **I** to **III** has 16 bits/pixel, which means that the camera can sense 65 536 shades of grey in each pixel. For the study presented in Paper **IV**, however, a 12 bit CCD was used. The interaction inside the vacuum chamber creates a lot of light and the laser beam is very intense, so an interference filter in front of the camera lens in combination with a light shield protects the camera. The setup can operate in two different modes, either together with a magnet to reveal the electron energy, or without to measure beam pointing and divergence. When operating without a magnet, simple trigonometry reveals the divergence and pointing of the electron beam, since the source is very small and can be considered to be point-like.

Electron Spectrometer

An electron traveling with velocity $\mathbf{v}$ through a magnetic field $\mathbf{B}$ will, due to the Lorentz force, experience a change in momentum, $\dot{\mathbf{p}} = q\,(\mathbf{E} + \mathbf{v} \times \mathbf{B})$. If there is no electrical field and using q_e as notation for the elementary charge, this expression reduces to $\dot{\mathbf{p}} = -q_e \mathbf{v} \times \mathbf{B}$. The work done on the electron by $\mathbf{B}$ over a curve

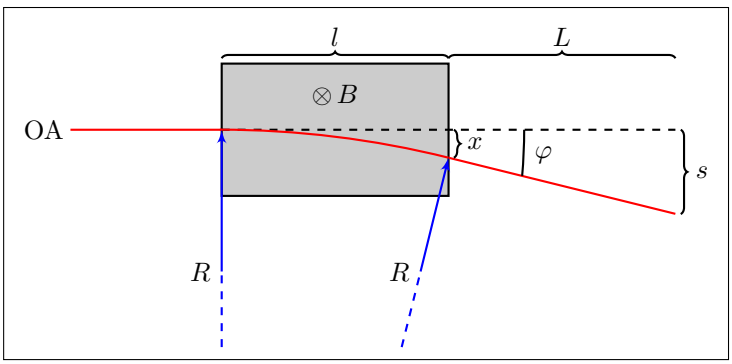

Figure 3.6. *The red line is the electron trajectory, with bending radius R inside the magnetic field. OA denotes the optical axis, which also is the initial path of the electron. The grey area represents a magnetic field pointing in to the paper. l is the length, in the propagation direction, of the magnetic field. s is the distance the electron has been deflected from OA after the length $l + L$.*

C is $W = \int_C \dot{\mathbf{p}} \times \mathrm{d}\mathbf{s} = 0$, since $\mathrm{d}\mathbf{s}$ is parallel to $\mathbf{v}$ and therefore orthogonal to $\dot{\mathbf{p}}$. Now, calculating the change of the electron energy, which equals W, yields $0 = \dot{E} = \mathrm{d}/\mathrm{d}t\left(\gamma m_e c^2\right)$, thus γ is constant in time and $\dot{\mathbf{p}} = \gamma m_e \dot{\mathbf{v}}$.

If $\mathbf{B}$ is constant and perpendicular to $\mathbf{v}$, the electron will travel in a circular arc since the force is orthogonal to both $\mathbf{B}$ and $\mathbf{v}$. The acceleration for a circular motion is $\dot{\mathbf{v}} = -\hat{\mathbf{e}}_v v^2/R$, where R is the radius of the circle traced by the moving electron and $\hat{\mathbf{e}}_v = \mathbf{v}/|\mathbf{v}|$. Thus, the bending radius for an electron in a constant magnetic field is

$$R \approx \frac{\beta E}{ceB}, \tag{3.1}$$

where $\beta = v/c \approx 1$ is the normalised speed.

To determine the distance, s, an electron has been deflected after a length $l + L$, it is helpful to consider Fig. 3.6. From the figure, it is obvious that $R^2 = l^2 + (R - x)^2$, or $x = R - \sqrt{R^2 - l^2}$. After the magnetic field, the electron will follow a straight trajectory, since it does not feel any forces. This means that $\tan(\varphi) = (s - x)/L$, and with some simple trigonometry, one can show that $\tan(\varphi) = l/(R - x)$. The combination of these equations yields

$$s = R - \sqrt{R^2 - l^2} + \frac{lL}{\sqrt{R^2 - l^2}}, \tag{3.2}$$

where R is given by Eq. 3.1.

From Eq. 3.2, we can define, for electrons in a certain energy range, two different types of magnets. One where $l > R$, which yields an imaginary solution of s. This means that the electron can not escape from the magnetic field, but is caught in a never-ending circular motion. This is, of course, not the physical reality, since an accelerating electron will emit radiation and loose energy, so R is not a constant. This is what could be called a strong magnet, since $R \propto B^{-1}$. The other case, $R \gg l$ yields $s \approx lL/R$. Often, $L \approx l$ which implies that s is very small. This is reasonable since

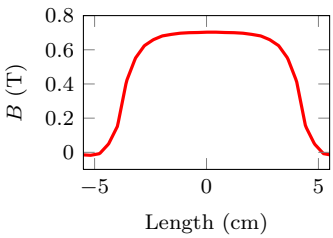

Figure 3.8. *Line-out of the magnetic field shown in Fig. 3.7. Gradients are visible on both sides of the maximum field strength.*

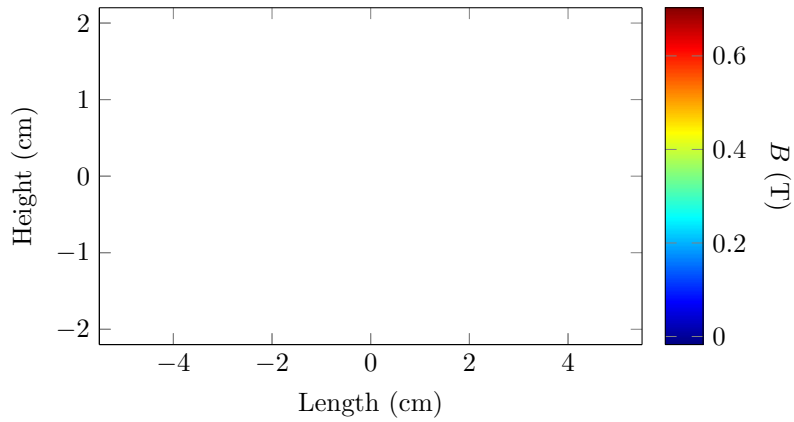

Figure 3.7. *The magnetic field strength of the magnet used in Papers **I** to **IV**. Note that the actual magnet is 12 cm with the iron cladding, but the map indicates an effective length of ∼10 cm. The size of the Hall probe also limits the height of the map to 4.4 cm, when the height of the actual magnet is 5cm.*

a large R indicates a low B or a very high E, which makes this a weak magnet for the electron energy E.

To determine which influence the distance L has on s, it is possible to calculate that

$$\frac{\partial s}{\partial L} = \frac{l}{\sqrt{R^2 - l^2}}. \tag{3.3}$$

For a magnetic field strength of 0.65 T and electron energy of 100 MeV, the bending radius is 0.5 m. If the length of the magnet is 10 cm, then $\partial s/\partial L = 0.25$. Thus, altering L by 1 cm changes s by 2.5 mm for this particular setup.

A map showing the magnetic field strength of the magnet we have used in experiments is shown in Fig. 3.7. The magnetic field is not constant over the entire magnet length, and the line-out in Fig. 3.8 shows that there are gradients several centimetres long in the field. Calculating an average effective magnetic field might be possible, but the best solution is to simulate the electron trajectories through this magnetic field. In this way, the effect of the magnet on highly divergent electron beams is possible to determine. The simulation can be implemented by a fourth-order Runge-Kutta method with a short time-step Δt_s, where the corresponding length $c_0 \Delta t_s$ should not exceed the resolution of the map of the magnet. Our magnetic field map has cells with lengths 0.48 mm in the direction of the optical axis, so a suitable time-step should be $\Delta t_s \leq 0.48\,\mathrm{mm}/c_0 \approx 1.6\,\mathrm{ps}$. The cell length in the perpendicular direction is 0.44 mm, and this also yields a time step of $\sim 1.6\,\mathrm{ps}$. In this way, the electron will feel the magnetic field in each cell as it propagates through it in the simulation.

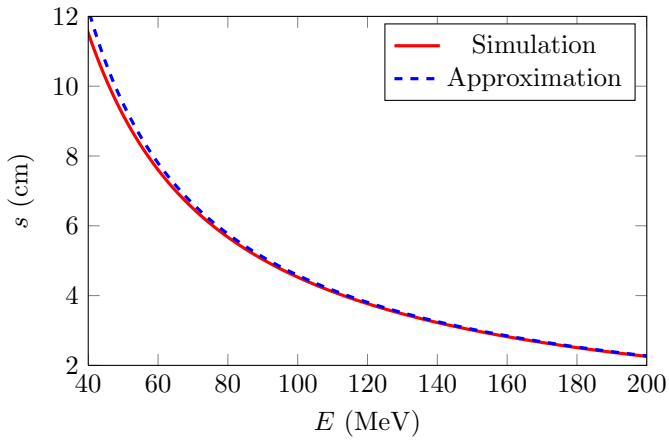

Figure 3.9. *Comparison between the simulated and constant-field approximated deflection. The approximation is based on a mean field strength of 0.52 T and length 10 cm.*

A comparison between the simulated dispersion and constant-field approximation is shown in Fig. 3.9. The simulation uses the actual map of the magnet shown in Fig. 3.7, while the constant-field approximation uses $l = 10\,\text{cm}$ and the mean magnetic field 0.52 T over that length. The difference for 100 MeV electrons are about 0.5 mm in s. This means that electrons measured to have the energy 100 MeV in the constant-field approximation actually have an energy of 98.8 MeV according to the simulation. This is an excellent agreement, so the constant-field approximation can be used for on-axis electrons. However, it is important to use an appropriate length for the approximation, which might not always be trivial to determine. Another important aspect of the approximation is that the magnetic field has to be centered around the optical axis, otherwise a different mean magnetic field must be used.

The lowest energy displayed in Fig. 3.9 is $\sim 40\,\text{MeV}$, which is the lowest detectable energy for the setup used during these simulations. In this case, the cut-off arises because the magnet has a height which is smaller than it's length, l, so electrons with $R \gtrsim l$ hit the magnet or it's iron cladding and are stopped. The cut-off can also be caused by letting L be very large. In this case, an electron that exits the magnet with an R just large enough to not hit it, could be bent too much and therefore miss the scintillating screen.

The spectrometer resolution is mainly limited by the beam divergence and pointing instabilities, and a typical resolution is displayed in Fig. 3.10. In the figure, a beam with 5 mrad uncertainty is plotted and ΔE is the energy range the beam can be interpreted as. As expected, the resolution is better at lower energies than at higher. The reason can be seen in Fig. 3.9. Since the dispersion is larger for lower energies, the resolution is higher when compared to higher electron energies.

[1] It is important to distinguish between counts on the CCD chip and counts in the image. It is common that images are saved in a 16-bit format, while the raw data itself is not 16 bit. For such images, a rescaling is needed so that one count on the CCD chip corresponds to one count in the image.

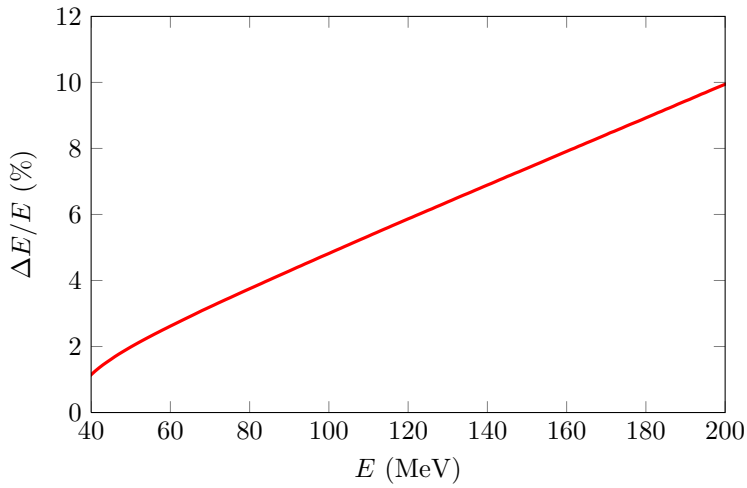

Figure 3.10. *Resolution for the spectrometer setup. In the simulation, an electron beam with 5 mrad divergence is evaluated using the same setup parameters as for Fig. 3.9.*

In Papers **I** to **III**, we present the accelerated charge in picocoulombs. This is partly done by measuring the quantum efficiency of the camera and estimating the solid angle of collection of the optical system. The conversion from CCD counts to absolute charge is energy-dependent, and is done by [31]

$$\frac{\mathrm{d}Q}{\mathrm{d}E}(E_0) = N(E_0) \times (\Lambda\,\Omega\,T_{\mathrm{total}}\cos\theta_{\mathrm{CCD}}\,\delta s_{\mathrm{pixel}})^{-1} \times \\ \times \left(\kappa \exp\left[-\frac{\tau_d}{\tau_l}\right]\right)^{-1} \times \cos\theta_{\perp}\frac{\mathrm{d}s}{\mathrm{d}E}, \tag{3.4}$$

where Q is charge and E is electron energy. The first factor of the right-hand side of Eq. 3.4 is the number of counts[1] on the CCD chip corresponding to an energy E_0, which is the actual signal of the measurement. The second factor depends on the geometry of the optical setup, where Λ is the number of CCD counts per recorded photon, Ω is the solid collection angle, T_{total} is the total transmission through all optics, θ_{CCD} is the viewing angle of the CCD camera and $\delta s_{\mathrm{pixel}}$ is the pixel size in the dispersion direction. The third factor depends on both the scintillator type (κ and τ_l), and the delay time, τ_d, which is how much of the signal that is cut out if time-gating of the camera is used. For a Kodak Lanex Regular screen, $\kappa = 6.95 \times 10^9\,(\mathrm{pC} \times \mathrm{sr})^{-1}$ [32] and $\tau_l = 660\,\mu\mathrm{s}$ [33]. The forth and last factor depends on the electron energy, where $\theta_{\perp}$ is the angle with which the electrons hit the scintillating screen, and $\mathrm{d}s/\mathrm{d}E$ is the energy dispersion. Dividing $\mathrm{d}s/\mathrm{d}E$ by $\delta s_{\mathrm{pixel}}$ yields the conversion between pixel size and the energy range. The setup-specific variables necessary for

Table 3.3. *The characteristics of the optical detection systems used in the studies presented in Papers **I** to **III***

Paper	Ω (msr)	q_{total}	θ_{CCD} (°)	τ_d (μs)	δs_{pixel} (μm)
I & **II**	0.963	0.49	43	0	13
III	0.840	0.45	40	76.5	4.65

the absolute charge calibration in Papers **I** to **III** are presented in Table 3.3.

An example of a raw electron spectrum image and it's evaluation is displayed in Fig. 3.11. A peaked spectra with a tail of lower-energy electrons is typical for laser wakefield acceleration experiments. The noise seen in the tail arise from three different sources. First, all CCD:s suffer from thermal noise, which means a cooled camera is preferred. The second source is residual light from the laser-matter interaction or the laser itself. One can either use time-gating, as was done for Papers **III** and **IV**, or a light-tight shield (Papers **I** and **II**). The advantage of using time-gating is that the experimental setup becomes much simpler. However, the downside is that the most intense part of the signal will be lost, which is not the case if a light-shield is utilised. The third, and probably largest, noise contributor is reflections of the scintillator light. Since the experiment takes place under vacuum, the light from the scintillator must pass through an experimental chamber window where light can be reflected. This means that a window of good optical quality with anti-reflection coating should minimise the noise. However, there are also other places where light can be reflected. One way to reduce it's influence on the resulting signal is to identify an area of the raw image where the main signal is not present. This area can then act as a measure of the reflections, as well as other noise, and then be subtracted from the rest of the raw image.

3.2.2 Interferometer

Consider two monochromatic plane waves, which are represented by their complex wave-functions $U_1 = \sqrt{I_0}\exp\left[-i\left(\mathbf{k}\cdot\mathbf{r}-\omega t+\varphi_1\right)\right]$ and U_2 defined similarly. The intensity, I, of their superposition is given by

$$I = \left|U_1 + U_2\right|^2 = 2I_0\left[1+\cos\left(\Delta\varphi\right)\right], \tag{3.5}$$

where $\Delta\varphi = \varphi_1 - \varphi_2$. Thus, the intensity of the superposition will be modulated by the phase difference.

If the two waves travel along paths with different refractive indices, η_1 and η_2, respectively, a phase difference between them

Table 3.4. *Phase differences, relative to vacuum, for light (λ = 632.8 nm) which have travelled 3 mm through different gases at standard pressure and temperature*

Gas	$\Delta\varphi$ (rad)
He	1.0
H_2	4.1
Ar	8.4

Table 3.5. *Refractive indices for helium, hydrogen gas and argon at standard pressure and temperature*

Gas	η
He	1.000 034 879
H_2	1.000 138 88
Ar	1.000 281 06

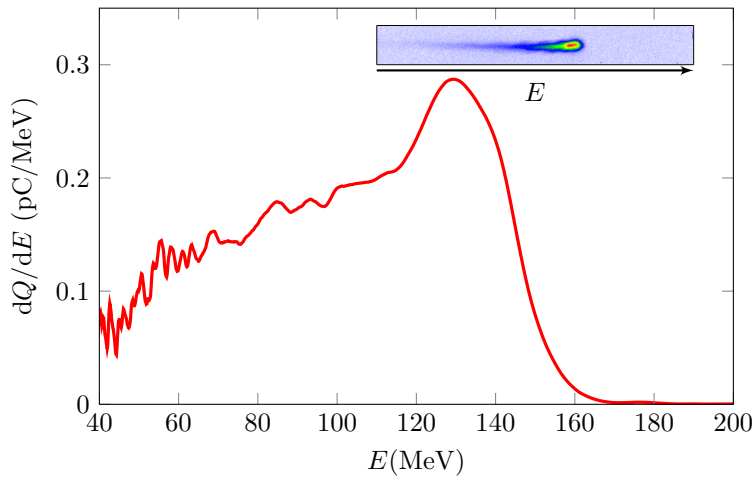

Figure 3.11. *A typical spectrum of laser wakefield accelerated electrons and the raw image as an insert. This spectrum has a peak at 130 MeV and the total detected charge is 20 pC. The detection setup has a lower energy threshold of 40 MeV and the highest detected energy is 155 MeV.*

is introduced. Assuming that the two different media are homogenous and that the wave's paths are parallel, the phase difference after a length d can be expressed as

$$\Delta\varphi = \frac{2\pi d\,(\eta_1 - \eta_2)}{\lambda}, \tag{3.6}$$

where λ is the wavelength. Therefore, measuring $\Delta\varphi$ and knowing d and λ together with one of the refractive indices, it is possible to determine the other. The phase differences relative propagation in vacuum calculated for $\lambda = 632.8\,\text{nm}$ and $d = 3\,\text{mm}$ for typical gases are displayed in Table 3.4. Their corresponding refractive indices are collected in Table 3.5.

Thus, by knowing how the refractive index of a medium changes with density, it is possible to determine it from the measured phase difference.

Our setup is an interferometer which is based on a birefringent Wollaston prism [34], and was an important part of Paper **II**. A schematic of this interferometer type is shown in Fig. 3.12. The interference is achieved by using an expanded polarised laser beam, and letting one part of it travel through a medium, while the other travels through a reference material, which in this case is vacuum. The beam is then lead through a Wollaston prism, which divides the beam into two parts with orthogonal polarisations and separated by an angle ϵ in space. Since the two parts of the beam now have orthogonal polarisations, they have to propagate through a polariser, which is oriented at a 45 ° angle to both of

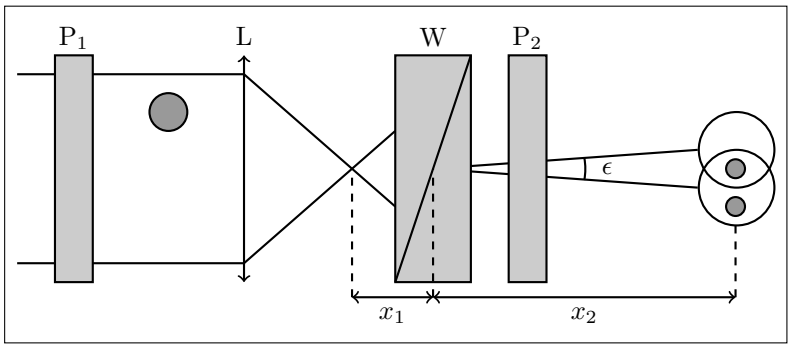

Figure 3.12. *The expanded linearly polarised beam enters from the left and the upper part aquires a phase shift as it is propagating through the gas, while the reference does not. The beam then passes through the imaging lens. The beam splitting is done in the Wollaston prism, where the light is divided into an ordinary and extra-ordinary ray. To get an interference pattern, another polariser is needed. The overlap of the two circles on the right represents the area where interference occurs. Note that the imaging plane has been rotated for viewing purposes.*

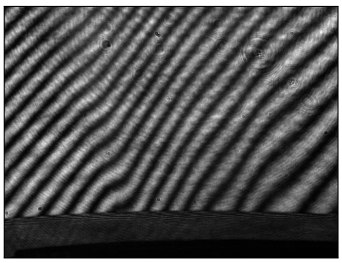

Figure 3.13. *Recorded interferogram in helium at 15 bar backing pressure.*

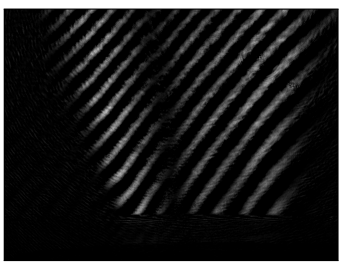

Figure 3.14. *Differential image of the interferogram in Fig. 3.13 and the unperturbed phase.*

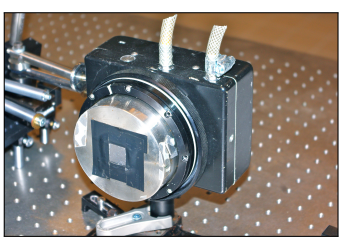

Figure 3.15. *The x-ray sensitive CCD camera used for detection of betatron radiation.*

them. The resulting interference pattern has a fringe separation of

$$\Delta = \frac{\lambda x_2}{\epsilon x_1}, \tag{3.7}$$

where ϵ, x_1 and x_2 are defined in Fig. 3.12. This means that the fringe separation can be changed by adjusting x_1 and x_2. The resulting density can then be retrieved from an Abel inversion of the interferogram, since the gas jet is cylindrically symmetric.

An example interferogram is displayed in Fig. 3.13, which is recorded using helium at 15 bar backing pressure. In Fig. 3.14, the same interferogram is shown with the reference phase subtracted, showing a clearly visible stream of gas.

The nature of this setup sets some restrictions on the illumination laser. Mainly, there is a need for a high spatial coherence and intensity uniformity of the laser beam, since different areas of the same wavefront interfere.

3.2.3 X-Ray Detection

The x-ray detection was, together with the electron spectrometer, the main diagnostics for Paper **III**.

As the electrons wiggle during the acceleration in the plasma they produce x-ray radiation, as presented in Section 2.3.4. A simple way to detect the spatial features of the x-ray beam is to use an x-ray sensitive CCD camera, as the one shown in Fig. 3.15, and place it in the beam path. However, the quantum efficiency of a CCD chip strongly depends on photon energy, so in this rather simple setup, no information of photon number is available.

This means that is is imperative to retrieve information of the photon energy as well. A filter array of different materials in front of the camera, and knowledge of the energy-dependent x-ray transmission through each of them, gives information of the spectral distribution of the x-ray beam. Then, by assuming a synchrotron-like spectrum, it is possible to determine the critical energy, E_c.

One problem with the x-ray detection is the influence of noise. The electrons that are accelerated in the plasma are deflected by a magnet and stopped in the chamber wall. During the deceleration, the electrons produce brehmstrahlung, which can hit the CCD. To reduce the influence of this radiation, the most obvious way is to build a dedicated electron beam dump, which minimises the amount of brehmstrahlung that reaches the x-ray sensitive CCD camera. Another way is to recognise that the betatron radiation is a collimated beam, whereas the brehmstrahlung will decrease as $1/L^2$, where L is the distance between the CCD and the beam dump. As long as the size of the x-ray beam is smaller than the CCD chip, the total amount of detected betatron radiation will be the same when L is increased. However, when the beam becomes bigger than the CCD chip, the amount of detected betatron radiation will start to decrease at the same rate as the brehmstrahlung. Thus, placing the x-ray sensitive CCD camera on axis, but far away from the experimental chamber will reduce the detected brehmstrahlung, and if the distance is not too great, the amount of detected betatron radiation will be the same. Another way of increasing the signal-to-noise ratio is to put the x-ray camera inside a lead enclosure, where a small hole on the optical axis lets the betatron radiation to be detected by the CCD.

Chapter 4

Summary of Experimental Results

*In this chapter, brief summaries of the experimental results of Papers **I** to **IV** are given.*

4.1 Influence of Gas Media on Electron Beam Quality in Laser Wakefield Accelerators

In this paper, we report an investigation of the difference between helium and hydrogen as interaction gas for laser wakefield acceleration experiments. The background for this experiment was the unexpected observation in the laboratory that electron beams emerging from hydrogen plasma seemed to be more stable than those from helium.

4.1.1 Experiment

The main diagnostic for this experiment was the electron detection setup which is described in detail in Section 3.2.1. During the experiment, a 3 mm gas jet produced the same number density of gas with hydrogen and helium, and since both have two electrons, the resulting electron density was the same for both gases. In this experiment the electron density was $n_e = 7.5 \times 10^{18}\,\mathrm{cm}^{-3}$ and the laser conditions are summarised in Table 4.1. To ensure a valid comparison, all data were collected during the same day, and continuos control of the laser energy ensured us that the laser parameters did not change during the experiment. Also, to ensure high purity, all tubes in the gas-handling system were completely evacuated each time when switching gases.

Table 4.1. *Laser parameters for Paper **I***

Laser Energy	1 J
Pulse Duration	37 fs
Spot Size (FWHM)	16 μm

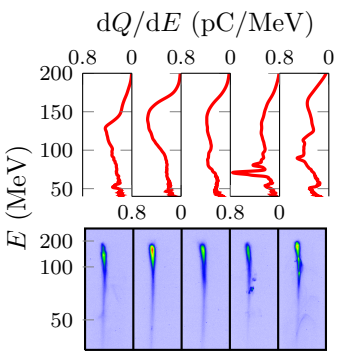

Figure 4.1. *Five consecutive electron spectra emerging from hydrogen. The images are representative for the entire series of shots. They are showing a stable behaviour and no high degree of filamentation.*

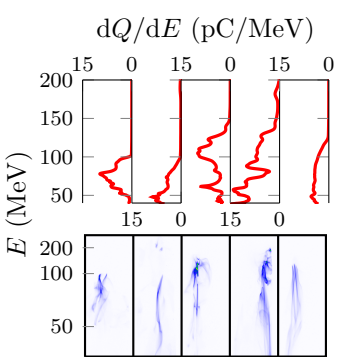

Figure 4.2. *Unlike the images in Fig. 4.1, these shots in helium are very unstable and electron beam filamentation is clearly visible.*

Table 4.2. *Summary of the experimental results. σ_{xy} and θ have the unit mrad, the unit of Q is pC, and E_m is given in MeV. $\langle a \rangle$ denotes the mean of a variable a, and $S(a)$ the corresponding standard deviation*

	H_2	He
$\langle \sigma_{xy} \rangle$	3.8	6.1
$S(\sigma_{xy})$	0.59	2.3
$S(\theta)$	5.1	9.8
$\langle Q \rangle$	50	120
$S(Q)$	15	41
$\langle E_m \rangle$	149	138
$S(E_m)$	28	29

4.1.2 Results

The results of the experiment can be visually summarised in two figures showing the electron spectra, Fig. 4.1 for hydrogen and Fig. 4.2 for helium. It is clear that the beams from helium suffer from a higher degree of filamentation and instabilities. For this reason the full width at half maximum (FWHM) beam divergence is not a good measure of the spread, and we instead use the two-dimensional standard deviation, $\sigma_{xy} = \sqrt{\sigma_x^2 + \sigma_y^2}$, of the electron beam profile images. σ_x^2 is defined as

$$\sigma_x^2 = \frac{1}{A} \iint_I (x - x_m)^2 \, I(x, y) \, \mathrm{d}x\mathrm{d}y, \tag{4.1}$$

where $I(x, y)$ is the raw image,

$$A = \iint_I I(x, y) \, \mathrm{d}x\mathrm{d}y \tag{4.2}$$

and

$$x_m = \frac{1}{a} \iint_I x I(x, y) \, \mathrm{d}x\mathrm{d}y. \tag{4.3}$$

σ_y is defined similarly. For a profile with a gaussian distribution, the FWHM divergence can be calculated as $\theta_{\mathrm{FWHM}} \approx 2.35\sigma_{xy}$. The results of this evaluation is shown in Fig. 4.3, and a large spread in σ_{xy} for helium is clearly noticeable. The electron beam pointing for both gases are displayed in Fig. 4.4. Again, a higher spread is seen for helium shots. A summary of the results of Paper **I** is presented in Table 4.2.

Several possible explanations for the difference in stability are considered in the paper. Helium has two ionisation stages, first He $\rightarrow$ He^+ and then $He^+ \rightarrow He^{2+}$. However, the intensities needed (see Table 2.1) for these ionisation steps are well below the peak intensity of the laser pulse, and should not influence the pulse evolution. The initial simulations we have done confirm this, since they showed no real difference of the laser-pulse evolution between helium and hydrogen. Another possible reason is ionisation at the edge of the plasma wave. It has been shown that the electrons that become trapped in the region behind the laser pulse, travel along the plasma wave edge [35], and if the laser pulse intensity is high enough to ionise He^+ to He^{2+}, additional electrons will be borne and captured by the wake. There is also possibilities of ionisation instabilities due to laser wavefront imperfections, not included in our initial simulations. The leading edge of the pulse, where the ionisation takes place, may be influenced by local ionisation defocusing and/or filamentation. Since we are working in a highly non-linear regime, initial imperfections in the wavefront will evolve during the laser pulse propagation. However, it is clear from our experimental data that electron beams emerging from

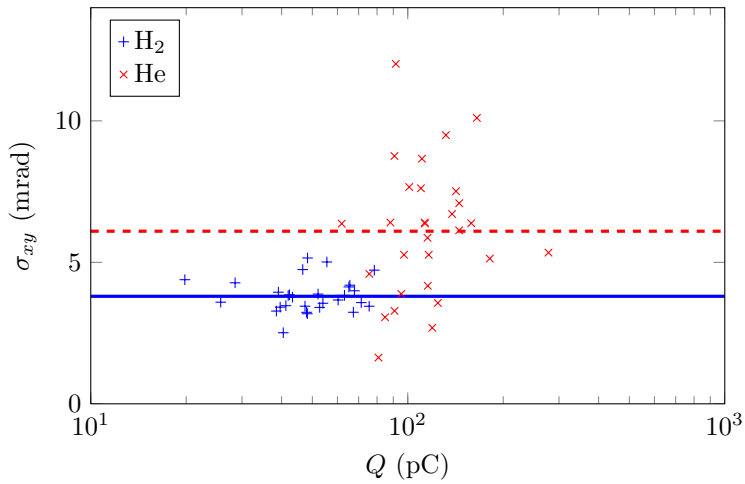

Figure 4.3. *The two-dimensional standard deviation of the recorded electron beam profiles. Results for hydrogen are shown as blue plus signs, and for helium as red crosses. The mean of σ_{xy} for the two gases are shown a solid blue line for hydrogen and a dashed red line for helium.*

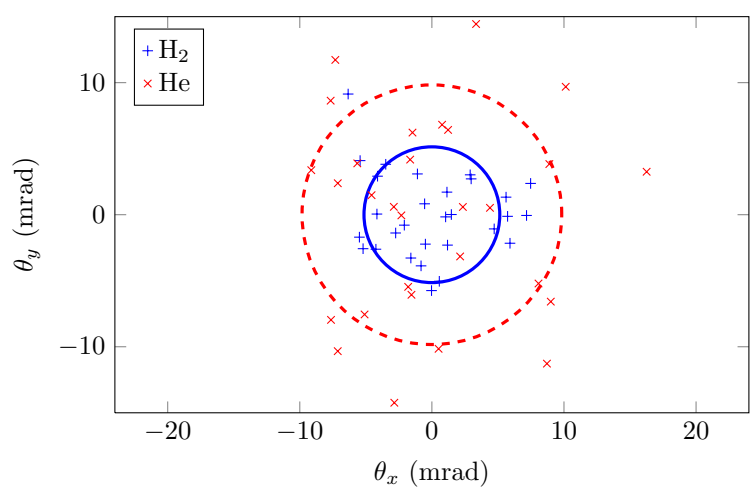

Figure 4.4. *The pointing of the electron beams are calculated as the weighted two-dimensional mean of the beam profile images. Shots in hydrogen are shown as blue plus signs and as red crosses for helium. The standard deviations for the two series are shown as a blue solid line and a red dashed line for hydrogen and helium, respectively.*

hydrogen have superior stability compared to those emerging from helium when it comes to important beam parameters.

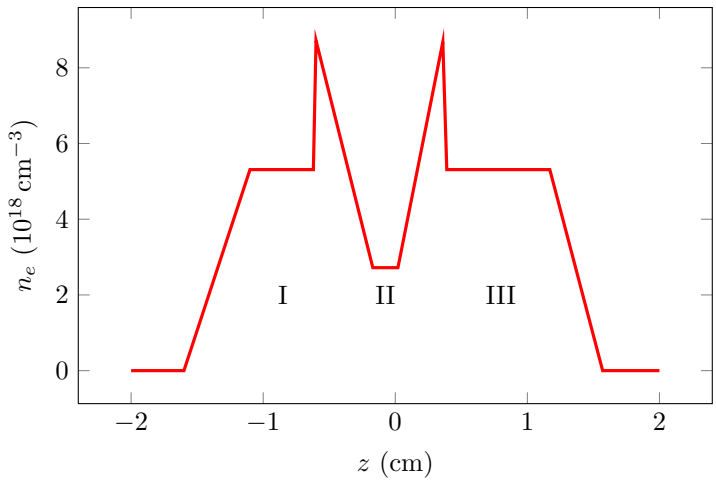

Figure 4.5. *The modulated density profile used for the simulations, which is a simplification of the actual measured density profile. Region I is where the laser pulse evolves to matched conditions before entering the density modulated region (II) where electrons are trapped in the plasma wave. After trapping, the plasma wave contracts as it enters region III where additional acceleration can occur.*

Table 4.3. *Laser parameters for Paper II*

Laser Energy	1 J
Pulse Duration	42 fs
Spot Size (FWHM)	16 μm

4.2 Staged Laser Wakefield Acceleration Using Double Density Ramps

The goal of this experiment was to implement density downramp injection by the simple means of introducing a thin wire in the gas flow, creating a region with lower density. The idea for this experiment came from an experiment where the gas density is modulated by introducing a razor blade into the gas flow [36]. However, by using a steel wire instead of a razor blade, the laser pulse can evolve to matched conditions before reaching the density-modulated region of the gas flow.

4.2.1 Experiment

The steel wire used in the experiment had a diameter of 25 µm, and was placed in the gas jet, between the optical axis and the 3 mm gas nozzle orifice. Interferometry done on the gas flow showed a modulation similar to the one in Fig. 4.5. It is possible to identify three distinct regions, denoted I, II and III, respectively, and their densities are $n_e^{(I)} = 6 \times 10^{18}\,\mathrm{cm}^{-3}$, $n_e^{(II)} = 3 \times 10^{18}\,\mathrm{cm}^{-3}$ and $n_e^{(III)} = 6 \times 10^{18}\,\mathrm{cm}^{-3}$ for a backing pressure of 9 bar. The length of region II is only ~ 300 µm, where the other two are of the millimetre scale. The backing pressures during the experiment spanned from 8 bar to 12.5 bar.

As diagnostics, the electron spectrometer was used to collect

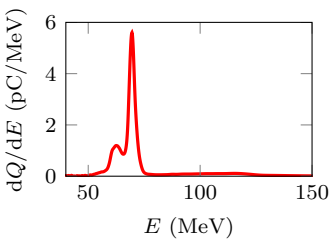

Figure 4.6. *A highly mono-energetic electron spectrum, peaked at 70 MeV. This spectrum has, for electrons with energy higher than 40 MeV, a total charge of 33.5 pC and a relative energy spread of 4.3 % (FWHM).*

information of electron beam charge and energy, as well as the divergence.

4.2.2 Results

The most apparent result was a dramatic decrease in relative energy spread, as well as electron beam divergence. An example electron spectra is displayed in Fig. 4.6. The relative energy spread is only 4.3 %, but as is seen in Fig. 3.10, a beam divergence of 5 mrad accounts for approximately 3.5 % of the spread at 70 MeV. This is quite remarkable, since the expected energy spread then is below 1 %. Energy spreads of this magnitude has only been achieved with other, more complicated, external injection mechanisms, such as colliding beams [37]. Over almost all of the scanned backing pressure range, the wire-injection method resulted in beams with ten times more charge than beams from self-injection, which is also remarkable.

It was also found that the resulting electron beam parameters were very sensitive to the wire position. The reason for this is that the laser pulse needs to evolve before entering region II, and also the fact that the length of this region is only $\sim 300\,\mu\text{m}$.

To get a picture of the physics behind the wire injection, we made simulations of the process. For the particle-in-cell (PIC) simulations, we used key parameters from the experiment, such as laser energy, focal spot size as well as a simplified density profile of the measured density map shown, in Fig. 4.5. The results showed that the acceleration mechanism can be separated into four different stages, where the first happens in region I. Here, the laser pulse evolves due to self-compression and relativistic self-focusing, without reaching wavebreaking.

When the laser pulse reaches the density gradient, the plasma wavelength is increased rapidly, which allows electrons between the first and second bucket to be trapped inside the first plasma wave period behind the pulse. This is expected, and has been reported on previously [38–40]. What happens next is, however, quite interesting. As the density is again increased, leading to region III, the simulation showed that the electron bunch is transferred to the second plasma wave period, due to the rapid decrease in plasma wavelength. There also appears to be some sort of filtering of the electron bunch, reducing the transversal spread of the individual electrons in the bunch. If the distance between the laser pulse and the electron bunch is assumed to be constant during this transition, it is possible to determine an optimal density ratio between region II and III, where the electrons end up in the accelerating phase of the second plasma wave period. This happens when $n_e^{(III)} \approx 4n_e^{(II)}$, which means that, according to

Eq. 2.12,

$$\lambda_p^{(II)} = \sqrt{\frac{n_e^{(III)}}{n_e^{(II)}}}\lambda_p^{(III)} = 2\lambda_p^{(III)}. \tag{4.4}$$

Letting the electron bunch accelerate in the second plasma wave period, instead of the first, eliminates any interaction between the laser pulse and the electron bunch [41]. This might also be one explanation to the observed decrease in beam divergence for this injection scheme.

It should also be noted that even though the optimal density ratio between the last two regions is 4, the laser pulse has to be able to propagate through the low-density region without too much diffraction for the acceleration in region III to take place.

The experimental results showed that our technique for staged laser wakefield acceleration yielded electron beams with very low spectral and spatial spread, as well as higher charge when compared to self-injected electrons. It is thus very interesting and will be further studied.

Table 4.4. *Laser parameters for Paper* ***III***

Laser Energy	1 J
Pulse Duration	40 fs
Spot Size (FWHM)	16 μm

4.3 Enhancement of X-Rays Generated by a Guided Laser Wakefield Accelerator inside Capillary Tubes

In this experiment, it was found that the generation of x-rays was enhanced when performing laser wakefield acceleration inside a capillary tube instead of a gas jet.

4.3.1 Experiment

During this experiment, the two main diagnostics were the electron spectrometer, with a detection limit at 42 MeV, and the x-ray sensitive CCD camera. Three different targets were used, where two were capillary tubes. They differed in length, l_c, and diameter, D_c, where the first had $l_c = 1.0$ cm and $D_c = 178$ µm and the second had $l_c = 2.0$ cm and $D_c = 152$ µm. The third target was a 2 mm super-sonic gas jet, which acted as a comparison reference. For all three targets, hydrogen was used as interaction gas.

4.3.2 Results

Previous studies [30, 42] have shown that the intense laser pulse can be guided over several centimetres inside capillary tubes, which allows energy outside of the full width at half maximum to be guided and avoid diffraction. This is not the case for a gas jet, as we found out in Paper **IV** and will be discussed in Section 4.4. The self-injection density threshold was found to be around 5.4×10^{18} cm^{-3} for the 1.0 cm tube, which, as expected for a low density, resulted in a low charge electron bunch with $Q < 1$ pC. Since there are few electrons, the generated x-ray fluence is also low. Increasing the density to 8.1×10^{18} cm^{-3}, resulted in more charge, and also brighter x-rays. The measured x-ray fluence generated by this electron bunch was 5.7×10^5 photons/mrad^2 and the spectrum had a critical energy of $E_c = 5.4$ keV. Using the longer (2.0 cm) capillary tube, it was found that the maximum x-ray fluence occurred at the same electron density. However, the stability of the measure fluence was better. This can be attributed to the improved laser guiding due to the smaller diameter of this capillary tube.

When the target was changed to a 2 mm gas jet, the electron density had to be increased for self-injection to occur. For this target, the maximum x-ray fluence, 2.7×10^4 photons/mrad^2, was measured at an electron density of 1.5×10^{19} cm^{-3}. The x-ray spectrum had a critical energy $E_c = 4.6$ keV. A possible reason for this difference lies in the laser-pulse guiding properties of the capillary, which enables the electron bunch to be accelerated over a longer distance at a lower electron density. This means that both the pump depletion length, defined in Eq. 2.21, as well as the

dephasing length, found in Eq. 2.15, will be longer than for a gas jet, letting the electrons accelerate to higher energies. This was detected as lower mean electron energies when using the gas jet instead of the capillary. The guiding of the laser pulse inside the tube also means that the local intensity can become higher than the initial intensity, which is also shown in simulations. The initial $a_0 = 1.6$ would in the 178 µm diameter capillary tube, evolve to $4 < a_0 < 5.5$. The simulations also showed that the laser-pulse evolution, injection and acceleration occurred over the first 10 mm inside the capillary, which reinforces the statement that the guiding is an important aspect of the injection and acceleration processes in capillary tubes.

Table 4.5. *Laser parameters for Paper* ***IV***

Laser Energy	≤ 0.7 J
Pulse Duration	≥ 40 fs
Spot Size (FWHM)	9.6 µm

4.4 Self-Injection Threshold in Self-Guided Laser Wakefield Accelerators

In this section, the results of a systematic study of the threshold for self-injection is discussed. More details are given in Paper **IV**. Before our study, it was believed that self-injection would occur at a fixed value of $\alpha P/P_c$, where α is the energy within the full width at half maximum of the focal spot, P the laser pulse power, and P_c the critical power for relativistic self-focusing, as defined in Eq. 2.19. During the study, we varied key variables and derived a new condition for the self-injection in laser wakefield accelerators.

4.4.1 Experiment

As stated in Section 3.1, the deformable mirror was important for this study, since we wanted to change α without altering the laser pulse power E_p. This was done by adding in a controlled way spherical aberration to the focal spot, moving energy out from the central part of the focal spot to the wings. It was important to have a symmetric spot, since an asymmetric focal spot affects the injection [43]. We also varied electron density, n_e, the energy in the laser pulse and the pulse length τ. All these variables could be changed independently of each other. E_p was altered by changing the pumping of the last amplification stage in the laser and τ by changing the grating separation in the laser pulse compressor. The pulse lengths were scanned between 40 fs and 80 fs. The 2 mm gas jet we used could produce electron densities up to $5 \times 10^{19}\,\mathrm{cm}^{-3}$, which could be varied by changing the backing pressure. During this experiment, we only used helium as interaction gas.

4.4.2 Results

It was found that changing α is equivalent to changing E_p, which is consistent with a self-injection threshold based on $\alpha P/P_c$. This also implies that the quality of the focal spot is very important for laser wakefield accelerators. However, altering τ and thus P, within the limits of our study, did not affect the self-injection threshold, which indicated that the laser-pulse compression, described in Section 2.3.7, plays a crucial role on the injection mechanism.

Our proposed explanation is that the laser-pulse compression will eventually produce the matched conditions needed for self-injection to occur. This allowed us to present an improved expression for the threshold as

$$\alpha E_p > \frac{\pi \epsilon_0 m_e^2 c^5}{e^2} \left[\ln\left(\frac{2n_c}{3n_e}\right) - 1 \right]^3 \frac{n_c}{n_e} \tau\left(l\right), \tag{4.5}$$

thus the important factor is the energy within the full width at half maximum of the laser focal spot. Our model fits accurately with our own experimental data, as well as previously presented data for laser systems with different pulse energies and pulse durations. By using Eq. 4.5, it is possible to determine the electron density needed to inject electrons into the plasma wave. However, knowledge about focal spot quality and acceleration length is required.

Chapter 5

Summary & Outlook

One of the main themes of my experimental work have been the stabilisation of the electron beam. It is important for future applications that the present fluctuations associated with electron beams generated by laser wakefield acceleration are reduced. As a comparison, the measured relative energy spread of the injected electrons in Paper **II** was found to be $< 4\,\%$ at an electron energy of 70 MeV. In the research field of laser wakefield acceleration, this is a remarkably low spread, but when compared to conventional accelerators, relative energy spreads $< 0.2\,\%$ (rms) are not uncommon. However, these accelerators are limited by electrical breakdown, which limits the accelerating electric fields to $\sim 10^2$ MV/m. In a plasma-based accelerator, no such breakdown exists, and the accelerating electrical field is $\sim 10^2$ GV/m. Thus, a possibility of a hugh reduction of size and cost for future electron accelerators could be achieved in the future by utilising laser wakefield acceleration.

As mentioned earlier in the thesis, there are several ways to improve the electron beam stability, where the most basic technique is presented in Paper **I**. By just choosing a different gas, we showed that the stability of important electron beam parameters can be increased by as much as 50 %. In Paper **II**, we also presented a technique to simultaneously increase charge and decrease divergence of the electron bunch by modulating the electron density. Paper **III** presented an increase of the x-ray fluence by using a capillary instead of the normally employed gas jet. The connection between these experiments are apparent; by letting the laser pulse remain constant, we enhanced the resulting electrons and x-rays by changes of the target. This is a good philosophy, the laser development will enable us to always increase the focused intensity which will increase the accelerated electron's energy, but if we can not control the interaction efficiently, there will always be large fluctuations in the resulting electron beam. Also, as we

showed in Paper **IV**, it is not only the energy of the laser pulse that is of importance for reaching the threshold for self-injection, but also the quality of the focal spot. To me, at least, this is a very good reason to continue the development of novel and better targets for laser wakefield acceleration.

Role of the Author

I have been one of the team in charge of operating the laser system during the experiments presented in Papers **I** to **IV**, as well as taking part in the experimental work. In all experiments, the multi-terawatt laser system at the Lund Laser Centre was used.

I **Influence of Gas Media on Electron Beam Quality**
The influence which the choice of gas has on the electron beam quality was investigated. Through a comparative study we showed that using H_2 as laser-matter interaction medium instead of He, commonly used previously by most groups, dramatically increased stability in the self-injection regime when using gas jets. I had a leading role in the experimental work and I did most data evaluation. I also wrote the manuscript.

II **Staged Laser Wakefield Acceleration Using Double Density Ramps**
The effect of density modulation by introducing a very thin steel wire in a supersonic gas flow was investigated. The results showed that the density modulation increased the charge yield and dramatically decreased the electron beam divergence. Simulations reinforces the physical description of the process. I took part of the experimental work, and had the main responsibility when evaluating electron spectra, which produced information about beam charge and energy distributions. I also gave constructive feedback on the manuscript.

III **Enhancement of X-Rays Generated by a Guided Laser Wakefield Accelerator inside Capillary Tubes**
Here, we reported on the findings that the betatron radiation generation from electrons accelerated inside a capillary tube was enhanced. The results showed an order of magnitude increase in the fluence of photons when comparing with betatron radiation generated in a gas jet plasma. I took part in the experimental work, mainly on the electron spectrometer. I evaluated all electron spectra, producing information on charge and energy distribution, and gave feedback on the manuscript.

IV **Self-Injection Threshold in Self-Guided Laser Wakefield Accelerators**
The wavebreaking threshold was studied by varying the quality of the focal spot, the energy in the pulse and the pulse duration. A simple model predicting if, and when, the wave would break was developed, showing good agreement with the experimental data. I took part in the experimental work and gave feedback on the manuscript.

Acknowledgments

First of all, I wish to thank my supervisor, Claes-Göran Wahlström, for giving me the opportunity to become a Ph.D. student in his research group. Your help, understanding and support have not gone unnoticed.

My co-supervisors, Olle and Anders, have also helped me a lot during my studies. Olle, with his great experience in laser wakefield acceleration and optics, has given me valuable experimental and theoretical guidance. Anders, who showed me the laser, always made sure we had enough laser power to accelerate electrons.

I also wish to thank past and present members of the research group: Guillaume and Matthias for all help when I was a newcomer. Frank for all the good times in the lab. Lovisa and Martin for continuing to accelerate particles in the basement.

I would also like to thank Stuart and Michael from Imperial College, who made my first electron acceleration campaign a blast.

All my best wishes to the French team, with which I had my first encounter with capillaries.

I also thank all my friends in Umeå for all the good times during my visits, which kept my mind occupied with other things than big lasers and fast electrons.

Thanks to my family for all support and especially to my sister, Malin, for pushing me to start an education in science instead of economics. Without you, this thesis would never have been written.

Dessutom, min underbara fästmö, Linda-Maria, för din förståelse för alla sena nätter, speciellt när den här licentiatavhandlingen skrevs. Sist, och inte minst, trots att du är minst Elisabeth, för att du gör varje dag till den bästa jag någonsin har haft.

References

1. T. Tajima and J. M. Dawson. *Laser Electron Accelerator.* Phys. Rev. Lett. **43**, 267–270 (1979).

2. D. Strickland and G. Mourou. *Compression of Amplified Chirped Optical Pulses.* Opt. Commun. **55**, 447–449 (1985).

3. A. Modena *et al. Electron Acceleration from the Breaking of Relativistic Plasma Waves.* Nature **377**, 606–608 (1995).

4. S. P. D. Mangles *et al. Monoenergetic Beams of Relativistic Electrons from Intense Laser-Plasma Interactions.* Nature **431**, 535–538 (2004).

5. C. G. R. Geddes *et al. High-Quality Electron Beams from a Laser Wakefield Accelerator Using Plasma-Channel Guiding.* Nature **431**, 538–541 (2004).

6. J. Faure *et al. A Laser–Plasma Accelerator Producing Monoenergetic Electron Beams.* Nature **431**, 541–544 (2004).

7. A. Pak *et al. Injection and Trapping of Tunnel-Ionized Electrons into Laser-Produced Wakes.* Phys. Rev. Lett. **104**, 25003 (2010).

8. C. McGuffey *et al. Ionization Induced Trapping in a Laser Wakefield Accelerator.* Phys. Rev. Lett. **104**, 025004 (2010).

9. J. Faure *et al. Controlled Injection and Acceleration of Electrons in Plasma Wakefields by Colliding Laser Pulses.* Nature **444**, 737–739 (2006).

10. C. G. R. Geddes *et al. Plasma-Density-Gradient Injection of Low Absolute-Momentum-Spread Electron Bunches.* Phys. Rev. Lett. **100**, 215004 (2008).

11. P. Gibbon. *Short Pulse Laser Interactions with Matter: An Introduction.* London: Imperial College Press (2005).

12. E. L. Clark *et al.* *Measurements of Energetic Proton Transport through Magnetized Plasma from Intense Laser Interactions with Solids.* Phys. Rev. Lett. **84**, 670–673 (2000).

13. R. A. Snavely *et al.* *Intense High-Energy Proton Beams from Petawatt-Laser Irradiation of Solids.* Phys. Rev. Lett. **85**, 2945–2948 (2000).

14. S. C. Wilks *et al.* *Energetic Proton Generation in Ultra-Intense Laser–Solid Interactions.* Phys. Plasmas **8**, 542 (2001).

15. W. Lu *et al.* *Generating Multi-GeV Electron Bunches Using Single Stage Laser Wakefield Acceleration in a 3D Nonlinear Regime.* Phys. Rev. Spec. Top. Accel. Beams **10**, 061301 (2007).

16. C. Rechatin *et al.* *Observation of Beam Loading in a Laser-Plasma Accelerator.* Phys. Rev. Lett. **103**, 194804 (2009).

17. E. Esarey *et al.* *Synchrotron Radiation from Electron Beams in Plasma-Focusing Channels.* Phys. Rev. E **65**, 056505 (2002).

18. S. Fourmaux *et al.* *Demonstration of the Synchrotron-Type Spectrum of Laser-Produced Betatron Radiation.* New J. Phys. **13**, 033017 (2011).

19. P. Sprangle, C.-M. Tang, and E. Esarey. *Relativistic Self-Focusing of Short-Pulse Radiation Beams in Plasmas.* IEEE Trans. Plasma Sci. **15**, 145–153 (1987).

20. G.-Z. Sun *et al.* *Self-Focusing of Short Intense Pulses in Plasmas.* Phys. Fluids **30**, 526 (1987).

21. J. Schreiber *et al.* *Complete Temporal Characterization of Asymmetric Pulse Compression in a Laser Wakefield.* Phys. Rev. Lett. **105**, 235003 (2010).

22. P. F. Moulton. *Tunable Solid-State Lasers.* Proc. IEEE **80**, 348–364 (1992).

23. D. E. Spence *et al.* *Regeneratively Initiated Self-Mode-Locked Ti:Sapphire Laser.* Opt. Lett. **16**, 1762–1764 (1991).

24. D. F. Hotz. *Gain Narrowing in a Laser Amplifier.* Appl. Opt. **4**, 527–530 (1965).

25. R. Y. Chiao, E. Garmire, and C. H. Townes. *Self-Trapping of Optical Beams.* Phys. Rev. Lett. **13**, 479–482 (1964).

26. P. L. Kelley. *Self-Focusing of Optical Beams.* Phys. Rev. Lett. **15**, 1005–1008 (1965).

27. J. E. Murray and W. H. Lowdermilk. *ND:YAG Regenerative Amplifier.* J. Appl. Phys. **51**, 3548–3556 (1980).

28. W. H. Lowdermilk and J. E. Murray. *The Multipass Amplifier: Theory and Numerical Analysis.* J. Appl. Phys. **51**, 2436–2444 (1980).

29. G. Genoud *et al. Laser-Plasma Electron Acceleration in Dielectric Capillary Tubes.* Appl. Phys. B: Lasers Opt. **105**, 309–316 (2011).

30. F. Wojda *et al. Laser-Driven Plasma Waves in Capillary Tubes.* Phys. Rev. E **80**, 66403 (2009).

31. Y. Glinec *et al. Absolute Calibration for a Broad Range Single Shot Electron Spectrometer.* Rev. Sci. Instrum. **77**, 103301 (2006).

32. A. Buck *et al. Absolute Charge Calibration of Scintillating Screens for Relativistic Electron Detection.* Rev. Sci. Instrum. **81**, 033301 (2010).

33. R. Nowotny and A. Taubeck. *A Method for the Production of Composite Scintillators for Dosimetry in Diagnostic Radiology.* Phys. Med. Biol. **54**, 1457–1468 (2009).

34. R. Benattar, C. Popovics, and R. Sigel. *Polarized Light Interferometer for Laser Fusion Studies.* Rev. Sci. Instrum. **50**, 1583–1586 (1979).

35. H.-C. Wu *et al. Electron Trajectories and Betatron Oscillation in the Wake Bubble in Laser-Plasma Interaction.* Phys. Plasmas **16**, 073108 (2009).

36. J. Faure *et al. Injection and Acceleration of Quasimonoenergetic Relativistic Electron Beams Using Density Gradients at the Edges of a Plasma Channel.* Phys. Plasmas **17**, 083107 (2010).

37. C. Rechatin *et al. Controlling the Phase-Space Volume of Injected Electrons in a Laser-Plasma Accelerator.* Phys. Rev. Lett. **102**, 164801 (2009).

38. S. Bulanov *et al. Particle Injection into the Wave Acceleration Phase Due to Nonlinear Wake Wave Breaking.* Phys. Rev. E **58**, R5257 (1998).

39. H. Suk *et al. Plasma Electron Trapping and Acceleration in a Plasma Wake Field Using a Density Transition.* Phys. Rev. Lett. **86**, 1011–1014 (2001).

40. R. G. Hemker, N. M. Hafz, and M. Uesaka. *Computer Simulations of a Single-Laser Double-Gas-Jet Wakefield Accelerator Concept*. Phys. Rev. Spec. Top. Accel. Beams **5**, 041301 (2002).

41. S. P. D. Mangles *et al.* *Laser-Wakefield Acceleration of Monoenergetic Electron Beams in the First Plasma-Wave Period*. Phys. Rev. Lett. **96**, 215001 (2006).

42. F. Dorchies *et al.* *Monomode Guiding of 10^{16} W/cm^2 Laser Pulses over 100 Rayleigh Lengths in Hollow Capillary Dielectric Tubes*. Phys. Rev. Lett. **82**, 4655–4658 (1999).

43. S. P. D. Mangles *et al.* *Controlling the Spectrum of X-Rays Generated in a Laser-Plasma Accelerator by Tailoring the Laser Wavefront*. Appl. Phys. Lett. **95**, 181106 (2009).

Papers

Paper I

Influence of Gas Media on Electron Beam Quality

K. Svensson, F. Wojda, M. Burza, G. Genoud, A. Persson, L. Senje, O. Lundh, and C.-G. Wahlström.

Manuscript in preparation.

Influence of Gas Media on Electron Beam Quality in Laser Wakefield Accelerators

K. Svensson, F. Wojda, M. Burza, G. Genoud, A. Persson, L. Senje, O. Lundh,[a)] and C.-G. Wahlström
Department of Physics, Lund University, PO Box 118, SE-221 00 Lund, Sweden

(Dated: 15th April 2012)

A comparative study of hydrogen and helium as medium for laser wakefield acceleration is presented. Higher stability in important electron beam parameters, such as charge, beam pointing and beam variance, is reported for hydrogen. The beam pointing fluctuations are reduced by 50 % when using H_2. The two-dimensional standard deviation of the beam charge distribution is decreased by 40 %. Electron beams emerging from the laser-matter interaction in H_2 have an average charge 60 % lower than beams from He, but the charge fluctuations are reduced by 65 %.

The use of high-intensity lasers as a mean for electron acceleration in underdense plasmas is an active area of research. It has been demonstrated that electron pulses, accelerated over short distances (∼mm), can achieve high energy, high charge, low relative energy spread, and small beam divergence[1–3]. The plasma can be created by focusing an intense laser pulse on the edge of a supersonic gas flow, where the front of the pulse ionises the medium. As the laser pulse is passing through the plasma, electrons are displaced by the ponderomotive force and creates a wake behind the pulse where trapped charge can be accelerated to high energies. The trapping can be done in several ways, where one of the simplest in practice is called self-injection. Here, the plasma wave is driven to high amplitude which causes it to break and plasma electrons to enter the accelerating fields in the wake.

Since self-injection of electrons into the wake is a highly non-linear process depending on the self-focusing and self-compression of the laser pulse, the shot-to-shot fluctuations are usually large. It is difficult to control the resulting characteristics of the beam, since it depends on multiple entangled parameters, such as longitudinal position of injection, effective acceleration length and amount of trapped charge, to name a few. Several research groups have investigated the influence of laser parameters on electron beam quality[4–6], and other recent techniques to improve the stability include colliding pulse injection[7], ionisation injection[8,9] and density-gradient injection[10]. However, the choice of gas for plasma creation has not been as extensively examined. The refractive index, η, in a plasma with multiple ionisation stages will have a gradient, since $\eta(r,t) \approx 1 - n_e(r,t)/2n_c$, where n_e is the number density of free electrons and n_c is the critical plasma density for laser propagation. A gradient in the refractive index will refract the laser, so usually low-Z elements such as He or H_2 are chosen to minimise the effect. However, due to its favourable chemical properties, He is commonly used instead of H_2 as gas medium for LWFA-experiments.

In this paper, we present a comparative study of H_2 and He as gas media, and investigate experimentally how the choice of gas influence the electron beam quality in the self-trapping regime. During the experiment, the Ti:Sapphire multi-TW laser system at the Lund Laser Centre (LLC) delivered 42-fs laser pulses at a 10 Hz repetition rate. This CPA system ($\lambda_0 = 800$ nm) delivered ~ 1 J per pulse on target. The 5-cm diameter beam is focused with a 75 cm focal length off-axis parabolic mirror to a 16 μm focal spot. This gives an estimated intensity of $\sim 10^{19}$ W/cm^2 in the focal plane and an associated initial normalised vector potential $a_0 \approx 1.7$, which after pulse compression[11] reaches ~ 2.4 if the interaction length is limited by pump depletion.

The target inside the experimental vacuum chamber is a supersonic jet of gas, which flows from a 3-mm diameter circular nozzle. A vacuum pump connected to the gas-handling system ensures that no mixing occurs when switching gases. The study is conducted at an electron density of 7.5×10^{18} cm^{-3}, which is taken to be twice the neutral gas density.

To detect the electron beam, a scintillating screen (Kodak Lanex Regular) is placed 38 cm from the gas nozzle in the laser forward direction. The setup can be operated in two different modes; either directly to determine electron beam spread and pointing stability, or with a permanent dipole magnet (length 12 cm and average field strength 0.65 T on the optical axis) to determine electron energies from the beam deflection. The optical system that images the Lanex screen is calibrated, which allows absolute charge in the electron beam to be determined[12,13]. The lowest detectable electron energy with this setup with magnet is ~ 40 MeV and the charge detection limit is ~ 1 pC.

A selection of electron profiles is shown in Fig. 1. As can be seen, many of the helium shots suffer from filamentation, which is why the full width at half maximum (FWHM) beam divergence is not a good measure of the beam spread. Instead, the two-dimensional standard deviation, σ_{xy}, of the images is used to quantify the beam profile quality. This technique takes into account the beam spread as well as any filamentation. The large difference in beam profile quality is seen directly in Figs. 1(c) and 1(d), where the average of 40 shots in H_2 and

[a)] Electronic mail: olle.lundh@fysik.lth.se

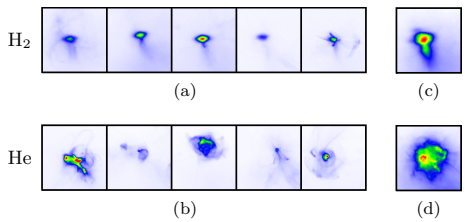

Figure 1. False-colour images of five consecutive shots in hydrogen (a) and helium (b). Due to the difference in total charge between the hydrogen and helium shots, the colour scale is different for the two series. On some shots, a dispersed tail can be seen. It is believed that these are low-energy electrons that are affected by fringe fields from the permanent magnet. The dipole magnet is removed from the optical axis, but remain inside the experimental chamber. (c) and (d) show the average electron beam profile for 40 shots in hydrogen and helium, respectively.

He, respectively, are shown. For H_2, the 40-shot average is similar to the individual shots seen in Fig. 1(a), which is not the case for He (compare Figs. 1(d) and 1(b)). Large fluctuations are also clearly visible in the electron spectra for He in Fig. 2(b). Again, beams originating in H_2 show a higher stability than those from He.

The pointing of electron beams accelerated in plasma produced from H_2, marked in blue in Fig. 3, experience a smaller spread than the ones from He (red). A good measurement of this stability is the standard deviation, $S(\theta)$, of the recorded shots' pointing. The results in Table I show a 50 % smaller $S(\theta)$ if H_2 is used instead of He for electron-beam generation. The higher stability is also visible in Fig. 4, where most images corresponding to beams from H_2 have $\sigma_{xy} < 5$ mrad. Beams from He, on the other hand, show beam charges about 140 % higher, but at the expense of more unstable beams. This is manifested in the average and deviation of σ_{xy}, which are 60 % and 290 % larger for He than for H_2, respectively. It is not only the actual beam charge that is higher for He than for H_2, as seen in Fig. 4 and Table I, the standard deviation in charge is also 40 % larger. The relative charge spread, however, is similar for both gases.

It should also be noted that the beams in Fig. 1(a) have an elliptical shape with the major axis oriented along the laser polarisation, which is a behaviour seen previously[14].

The spread in charge is much larger for He in Fig. 4 compared to Fig. 3, which is partly due to the energy detection threshold, i.e. electrons with energies lower than 40 MeV do not contribute to the detected charge. There are also some beams with very high charges (> 500 pC). However, no significant difference is found relating to the highest measured electron energy, E_m, between to the different gases.

In this paper, it has been shown that choosing H_2 as target gas for LWFA dramatically increases the stability of important electron beam parameters, such as pointing,

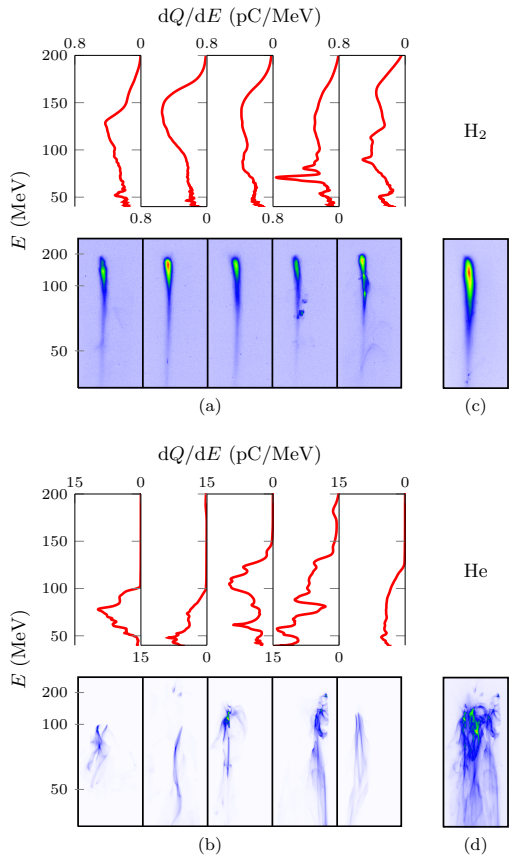

Figure 2. (a) and (b) show false-colour images of five consecutive electron spectra recorded with hydrogen and helium, respectively. Higher degree of filamentation and pointing instability in helium is clearly visible. To emphasise the difference in shot-to-shot fluctuations, the average of 40 shots is shown in (c) and (d). The average of the hydrogen shots, (c), resembles the individual shots, which is not the case for helium as seen in (d). Due to the large difference in electron beam charge, the colour scale is not the same in the different series.

Table I. Summary of results. $\langle f \rangle$ denotes the mean value of a variable f and $S(f)$ the corresponding standard deviation. Due to the cut-off of charge when operating in the spectrometer mode of the setup, only shots without are used when determining the charge of the electron beam.

Gas	$\langle \sigma_{xy} \rangle$ (mrad)	$S(\sigma_{xy})$ (mrad)	$S(\theta)$ (mrad)	$\langle Q \rangle$ (pC)	$S(Q)$ (pC)	$\langle E_m \rangle$ (MeV)	$S(E_m)$ (MeV)
H_2	3.8	0.59	5.1	50	15	149	28
He	6.1	2.3	9.8	120	41	138	29

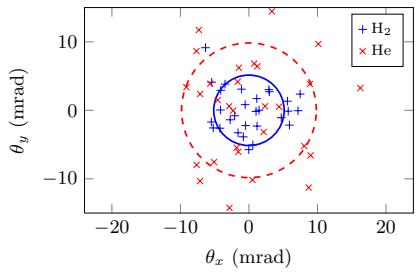

Figure 3. The data points are centred around their mean values. The standard deviation of the pointing is shown as solid (hydrogen) and dashed (helium) circles.

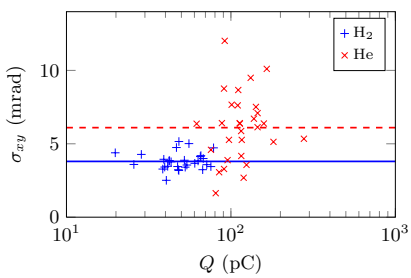

Figure 4. The two-dimensional standard deviation of the beam charge distribution is compared with the total beam charge.

charge and beam variance. The two-dimensional standard deviation is reduced by 40 % and pointing fluctuations by half. The charge in the electron beam is 60 % lower for H_2 compared to He, but the fluctuations are decreased by 60 %. No significant difference in maximum electron energy between beams from the different gases is noticed.

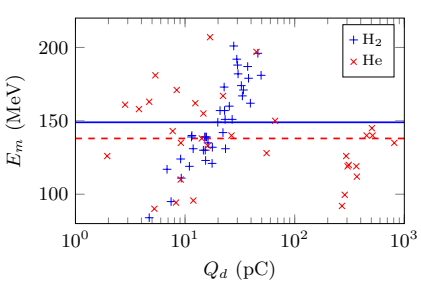

Figure 5. Detected beam charge of electrons with energy > 40 MeV as a function of highest electron energy. The data points for helium have again a larger charge spread. The mean of the maximum energy has been marked by solid (hydrogen) and dashed (helium) lines.

The authors acknowledge the financial support from the Swedish Research Council (including the Linné grant to Lund Laser Centre) and the Knut and Alice Wallenberg Foundation.

[1] J. Faure, Y. Glinec, A. M. P., S. Kiselev, S. Gordienko, E. Lefebvre, J.-P. Rousseau, F. Burgy, and V. Malka, Nature **431**, 541 (2004).

[2] C. G. R. Geddes, C. S. Toth, J. van Tilborg, E. Esarey, C. B. Schroeder, D. Bruhwiler, C. Nieter, J. R. Cary, and W. P. Leemans, Nature **431**, 538 (2004).

[3] S. P. D. Mangles, C. D. Murphy, Z. Najmudin, A. G. R. Thomas, J. L. Collier, A. E. Dangor, E. J. Divall, P. S. Foster, J. G. Gallacher, C. J. Hooker, D. A. Jaroszynski, A. J. Langley, W. B. Mori, P. A. Norreys, F. S. Tsung, R. Viskup, B. R. Walton, and K. M. Krushelnick, Nature **431**, 535 (2004).

[4] S. P. D. Mangles, A. G. R. Thomas, O. Lundh, F. Lindau, M. C. Kaluza, A. Persson, C.-G. Wahlström, K. M. Krushelnick, and Z. Najmudin, Phys. Plasmas **14**, 056702 (2007).

[5] N. M. Hafz, I. W. Choi, J. H. Sung, H. T. Kim, K. H. Hong, T. M. Jeong, T. J. Yu, V. Kulagin, H. Suk, Y. C. Noh, D. K. Ko, and J. Lee, Appl. Phys. Lett. **90**, 151501 (2007).

[6] S. P. D. Mangles, A. G. R. Thomas, M. C. Kaluza, O. Lundh, F. Lindau, A. Persson, Z. Najmudin, C.-G. Wahlström, C. D. Murphy, C. Kamperidis, K. L. Lancaster, E. J. Divall, and K. M. Krushelnick, Plasma. Phys. Contr. F. **48**, B83 (2006).

[7] J. Faure, C. Rechatin, A. Norlin, A. F. Lifschitz, Y. Glinec, and V. Malka, Nature **444**, 737 (2006).

[8] C. McGuffey, A. G. R. Thomas, W. Schumaker, T. Matsuoka, V. Chvykov, F. J. Dollar, G. Kalintchenko, V. Yanovsky, A. Maksimchuk, K. Krushelnick, V. Y. Bychenkov, I. V. Glazyrin, and A. V. Karpeev, Phys. Rev. Lett. **104**, 025004 (2010).

[9] A. Pak, K. A. Marsh, S. F. Martins, W. Lu, W. B. Mori, and C. Joshi, Phys. Rev. Lett. **104**, 025003 (2010).

[10] C. G. R. Geddes, K. Nakamura, G. R. Plateau, C. Toth, E. Cormier-Michel, E. Esarey, C. B. Schroeder, J. R. Cary, and W. P. Leemans, Phys. Rev. Lett. **100**, 215004 (2008).

[11] J. Schreiber, C. Bellei, S. P. D. Mangles, C. Kamperidis, S. Kneip, S. R. Nagel, C. A. J. Palmer, P. P. Rajeev, M. J. V. Streeter, and Z. Najmudin, Phys. Rev. Lett. **105**, 235003 (2010).

[12] Y. Glinec, J. Faure, A. Guemnie-Tafo, V. Malka, H. Monard, J. P. Larbre, V. De Waele, J. L. Marignier, and M. Mostafavi, Rev. Sci. Instrum. **77**, 103301 (2006).

[13] A. Buck, K. Zeil, A. Popp, K. Schmid, A. Jochmann, S. D. Kraft, B. Hidding, T. Kudyakov, C. M. S. Sears, L. Veisz, S. Karsch, J. Pawelke, R. Sauerbrey,

T. Cowan, F. Krausz, and U. Schramm, Rev. Sci. Instrum. **81**, 033301 (2010).
[14]S. P. D. Mangles, A. G. R. Thomas, M. C. Kaluza, O. Lundh, F. Lindau, A. Persson, F. S. Tsung, Z. Najmudin, W. B. Mori, C.-G. Wahlström, and K. Krushelnick, Phys. Rev. Lett. **96**, 215001 (2006).

Paper II

Staged Laser Wakefield Acceleration Using Double Density Ramps

M. Burza, A. Gonoskov, K. Svensson, F. Wojda, A. Persson, M. Hansson, G. Genoud, M. Marklund, C.-G. Wahlström, and O. Lundh.

Manuscript in preparation.

Staged Laser Wakefield Acceleration Using Double Density Ramps

M. Burza,[1] A. Gonoskov,[2,3] K. Svensson,[1] F. Wojda,[1] A. Persson,[1] M. Hansson,[1]
G. Genoud,[1] M. Marklund,[2] C.-G. Wahlström[1] and O. Lundh[1]

[1] *Department of Physics, Lund University, P.O. Box 118, SE-221 00 Lund, Sweden*
[2] *Department of Physics, Umeå University, SE-901 87 Umeå, Sweden*
[3] *Institute of Applied Physics, Russian Academy of Sciences, 46 Ulyanov Street, Nizhny Novgorod 603950, Russia*
(Dated: April 13, 2012)

A novel approach to implement and control electron injection into the accelerating phase of a laser wakefield accelerator (LWFA) is presented. It utilizes a wire, which is introduced into the flow of a supersonic gas jet, creating shock waves and three stages of differing but nearly constant plasma density. As a result, electron acceleration takes place in four separate stages: Laser self-compression, injection, bunch transfer into the second bucket of the plasma wake and acceleration. Compared to self-injection by wavebreaking of a nonlinear plasma wave in a constant density plasma, this novel wire injection scheme increases beam charge by up to one order of magnitude. Electron acceleration in the second bucket reduces electron beam divergence by $\approx 25\,\%$, while resulting in quasi-monoenergetic spectra with $\lesssim 1\,\%$ relative spread due to the highly localized injection at the density downramp shock wave.

In plasma based laser driven electron accelerators, high longitudinal field strengths of the order $> 100\,\mathrm{GV/m}$ can be sustained in the plasma oscillation produced in the wake of an intense laser pulse [1]. This allows for short acceleration lengths and together with the relatively compact high power table top laser systems readily available [2] give an advantage over conventional accelerators using RF cavities.

In most experiments, injection of electrons into the accelerating structure relies on breaking of the plasma wave, which then can self-inject electrons. This scheme is rather simple and quasi-monoenergetic beams have been produced in this way [3–5]. Electron beams of low spectral spread and divergence are necessary in order for these accelerators to be attractive for applications [6–8]. However the wavebreaking process is highly nonlinear and in order to achieve higher quality beams, means of controlling the injection process are necessary. Both, charge and instant of electron injection from the background plasma into the accelerating and focusing phase of the wakefield are crucial [9–11]. In this respect self-injection [12–14] is inferior to most schemes with external injection control, such as colliding pulse techniques [15–18], ionisation injection [19, 20] or density gradients [21–23]. The research presented in this article involves the third named type of controlled injection. In this case, at the downwards gradient the plasma wavelength is increased rapidly enough for the plasma wave to break as a result of the wave phase irregularity created at the transition.

A shock wave and thus a very abrupt density transition has been produced by introducing a knife edge into a supersonic gas flow [24]. With the driving laser aiming close to the blade, a well defined plasma boundary, followed by a shock wave and a downwards gradient will be encountered by the laser. Alternatively, an auxiliary pulse may produce an electron depleted region by a formation of an ionisation channel followed by hydrodynamic expansion [25, 26]. Our experiment relates to those as we modulate plasma densities along the laser propagation axis to control injection externally.

We believe that a thin wire, as a novel tool, introduced into a gas jet, can produce an extremely sharp electron density downramp for gradient injection due to the only some microns thick boundary layers that are available in supersonic shock waves [27]. Laser plasma machining, which requires accurate spatial and temporal overlap with a second laser pulse, may suffer from ionisation defocusing, and ionises electrons corresponding to the auxiliary laser's radial intensity profile, which varies over beam diameter. After hydrodynamic expansion, the density modulation will be fundamentally different from the modulation produced by a wire and may be less steep. Another advantage of the wire is the possibility for the pulse to propagate in the undisturbed plasma prior to reaching the shock waves. It has time to match itself to the experimental conditions by relativistic self-focusing, self-modulation and compression by nonlinear interaction with the plasma without significant trapping to take place (stage 1). A knife edge, which is also capable of producing extremely sharp shock wave gradients, lacks the amount of control to independently adjust position and density ratios before and after the shock wave, where localized injection is supposed to occur (stage 2). Our method combines advantages of both setups, while circumventing the rigidity of the knife edge setup and the inherent increased complexity of two beam experiments. However besides enabling stage 1 and 2 in one single experiment, a key feature of the wire injection scheme, never utilized before, is a controlled charge transfer of the injected electron bunch from the first into the second bucket of the plasma wake oscillation. This is accomplished by a rapidly shrinking plasma wavelength at a proceeding shockwave upramp (stage 3). This filters the already injected bunch and isolates it from the laser field during acceleration (stage 4), improving its longitudinal and transverse emittance. Ingeniously, stage 4 is driven by the same already matched laser pulse from stage 1. The wire injection scheme presented in this article is thus a novel, staged, four step, laser wakefield accelerator.

The experiment was conducted at the Lund Laser Centre,

Sweden, where a Ti:Sa CPA laser system provides pulses at 800 nm central wavelength with 42 fs duration at an energy of approximately 1 J on target. A deformable mirror provides a nearly diffraction limited focal spot with of an $f/15.5$ off-axis parabolic mirror $\sim 700\,\mu$m above the orifice of a 3 mm diameter supersonic gas nozzle, which provides the target gas. The laser is focused on the entry density upramp of the gas jet boundary producing a spot with $\approx 9.3\,\mu$m intensity FWHM diameter. A wire is spanned and positioned over the nozzle but below the laser interaction area by a motorized holder. This produces three distinct plasma density regions for the laser interaction (see white broken line function in Fig. 5 b)), separated from each other by shock waves. Interferometric measurements of plasma densities are carried out using hydrogen at 9 bar backing pressure. Densities scale linearly with backing pressure. Initially the laser pulse encounters a region of constant density (region I), which has been determined to $\approx 6\times10^{18}\,\mathrm{cm}^{-3}$. After ~ 1 mm it encounters the first shock wave and downwards gradient, which is expected to be $\leq 20\,\mu$m as suggested by [28]. Here in region II, the plasma density is reduced to only $\approx 3\times10^{18}\,\mathrm{cm}^{-3}$ for $\sim 300\,\mu$m. After that, the second shock wave is encountered followed by region III, which provides a similar density plateau as in region I but at a different length, until the end of the gas jet is reached. By adjustments of wire position, thickness and Mach number, gradients and density ratios between region I and II can be tailored to match the requirements for electron injection and laser guidance. Shock wave divergence angle and density ramps have been found to be symmetric as long as the wire is < 0.5 mm off the nozzle centre. If no wire is present, the plasma density is comparable to that at the plateau regions I and III.

As diagnostics serve a top view camera as well as a permanent magnet electron spectrometer quipped with a Lanex screen (Kodak Lanex Regular), whose emission is recorded by a 16 bit CCD camera. Based on previous work [29, 30] the electron spectrometer is calibrated in absolute charge. The setup is depicted in Fig. 1.

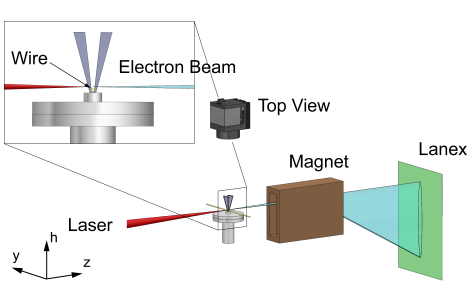

FIG. 1: Experimental setup: The laser pulse arriving from the left impinges on the gas jet ≈ 0.7 mm above the nozzle. The wire is positioned ≈ 0.2 mm above nozzle rim. Top view and a permanent magnet Lanex electron spectrometer serve as primary diagnostics. The origin (h,y,z=0) is centred above the nozzle at laser height

Stainless steel wires with $300\,\mu$m, $200\,\mu$m, $50\,\mu$m and $25\,\mu$m diameter have been tested, but only the latter two stimulate injection, with a much improved performance of the $25\,\mu$m wire. Thicker wires inevitably increase the density diluted region II both in depth and width, promoting diffraction and making it difficult to maintain a sufficiently strong laser driver in the second high density region. Hydrogen and helium have both been tested as target gas but with the wire present, only hydrogen produced electron beams.

A wire height scan reveals increased probability for the wire injection scheme to work with reduced distance. However, closer than $h = -0.65$ mm dramatically reduces the wire's lifetime. As no improved performance on the production of electron beams can be observed between $h = -0.35$ mm to $h = -0.50$ mm, the latter position is chosen.

A z-scan conducted with the $25\,\mu$m wire at $h_{opt} = -0.50$ mm and a backing pressure around the threshold for self-injection reveals the sensitivity of the wire position on the production of electron beams (threshold is defined here as plasma density resulting in beams with $< 10\,\%$ of the maximum charge observed during a pressure scan). This window is found to be $\sim 200\,\mu$m wide only. Outside this, beam charge is comparable to the self-injection case without density modulation.

Pressure scans are carried out at what has been found to be the optimum spatial parameters: $d_{opt} = 25\,\mu$m, $h_{opt} = -0.50$ mm, $z_{opt} = -0.07$ mm. The wire injection scheme is found to be rather robust with regard to backing pressure. Below the self-modulated LWFA regime at ≈ 11 bar, beam charge is increased by one order of magnitude, as shown in Fig. 2. Divergence during wire injection seems to be unaffected by the pressure but is on average only 75 % of the value encounterd in the self-injection case.

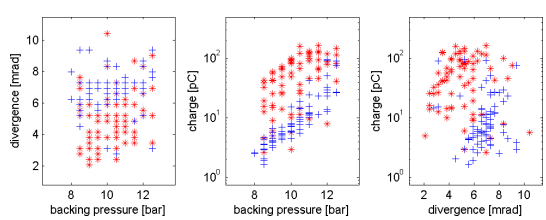

FIG. 2: Comparison of divergence, charge and brightness of electron beams with the wire at $h_{opt} = -0.5$ mm (red stars) as compared to nonlinear wavebreaking and self-injection LWFA (blue crosses). Every data point corresponds to one shot. Failure rate with wire is below 5 % and thus comparable to the wireless self-injection process

Example spectra can be seen in Fig. 3, showing the spectral range from ~ 43 MeV to infinity. The effects of the wire are threefold: It injects a charge ~ 10 times higher than that available without wire while at the same time providing beams with a quasi-monoenergetic spectra and reduced divergence, thus brightness is increased dramatically. A weak self-injected background charge can be identified in most of

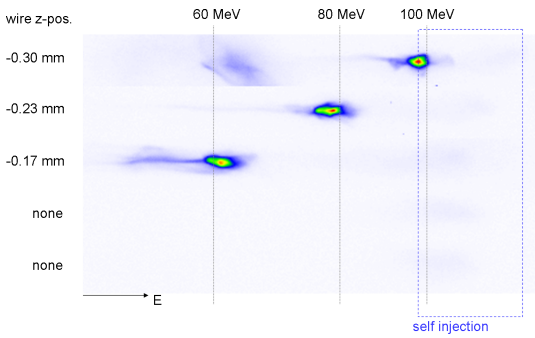

FIG. 3: Example spectra with comparable charge and variable wire position as recorded on the Lanex screen using 9.5 bar backing pressure. Besides the rather strong peak when the wire is present, weak background self-injection can be seen in all spectra.

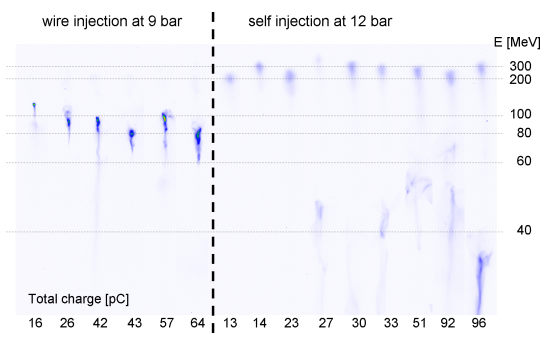

FIG. 4: Example spectra of beams with variable charge and fixed wire position; left: wire injection at 9 bar backing pressure; right: self-injection at 12 bar backing pressure to compensate for the charge increase in the wire injection case as indicated in Fig. 2; each group has been sorted according to integrated charge

the shots. Within limits, energy tuning is possible by altering the wire's z-position (Fig. 3). From this a field gradient of ~ 250 GV/m may be estimated.

From the same data, a relative spectral spread $\frac{\Delta E}{E} \leq 4\,\%$ can be calculated. Note however, that spectrometer dispersion and divergence have not been deconvoluted here. In fact, 4 mrad divergence (see Fig. 2) produces an apparent $\frac{\Delta E}{E} \approx 4\,\%$ at 100 MeV, thus the real relative spectral spread is expected to $\lesssim 1\,\%$. Electron beam mean energies are generally lower with wire but are compensated for by improved beam quality.

Fig. 4 compares spectra with and without wire at backing pressures, such that the resulting beam charge is comparable for both cases. Thus self-injection at 12 bar backing pressure is compared to wire injection at 9 bar. The tendency of decreasing peak energy with increasing charge due to beam loading [10], which is clearly visible in the wire injection case, indicates that injection probably still occurs at the same z-position.

The 3D fully relativistic parallel PIC code *ELMIS* [31] is used to investigate the physical mechanisms responsible for the experimentally observed phenomena. Key parameters are taken from the experiment with the plasma densities approximated by a broken-line function mirroring the interferometric density data and with gradients ($\sim 20\,\mu$m) as motivated earlier. 140 attoseconds correspond to one time step in the simulation and an $80\,\mu\text{m}\times 80\,\mu\text{m}\times 80\,\mu\text{m}$ box is represented by $1024 \times 256 \times 256$ cells. The ions (H^+) are mobile. During the simulation the average number of virtual particles of both types is 0.5 billion.

When traversing the first high density area (region I in Fig. 5), the laser pulse gets focused transversely and generates a highly nonlinear plasma wave, which nevertheless does not reach breaking and thus neither provides longitudinal nor transverse electron self-injection. In line with previous studies [21, 23, 32] at the density downramp, the leading cavity of the nonlinear plasma wave rapidly expands behind the laser pulse and thereby catches electrons accumulated between the first and the second bucket. In region II these electrons form an electron bunch. At the entry to the second high density area (region III), the cavity size rapidly shrinks so that the generated electron bunch is moved to the second bucket but not necessarily to its accelerating phase. Therefore electrons may now decelerate and fall further behind until they reach the acceleration phase of the second bucket, as depicted in Fig. 5 a).

We can state the following new aspect of this staged electron acceleration concept: If the distance between the laser pulse and the electron bunch remains constant while passing the density upramp, the size of the plasma cavity in the high density region should ideally be half the size of what it has been in the low density region in order to match acceleration phases. Thus densities should roughly differ by a factor four under the premise that either the laser pulse can traverse region II with sufficient guiding by the plasma or region II being sufficiently short. However, the allowed density regime is not too sensitive to actual plasma densities and gradients. For the case of non-matched wire injection conditions, electrons in region III may first decelerate but eventually they will reach the proper position for further acceleration.

The initial dephasing of injected electrons entering the second high density region, followed by a rapid acceleration over no more than half a millimetre, where the gas jet ends, explains the rather short acceleration lengths that can be deduced from the field estimates related to Fig. 3. This also leads to the observed lower final energy of the electrons compared to the self-injection case. At the same time it explains why electron acceleration can only be observed when laser interaction takes place at a certain distance to the wire as this affects the encountered density ratios. Should the electrons due to a density mismatch end up in the decelerating phase and not manage to reach the accelerating phase before the end of the gas jet, no beams of high energy electrons are observed. This is what happens with helium, which could not provide suitable ratios as a result of its fluid characteristics, while working with sim-

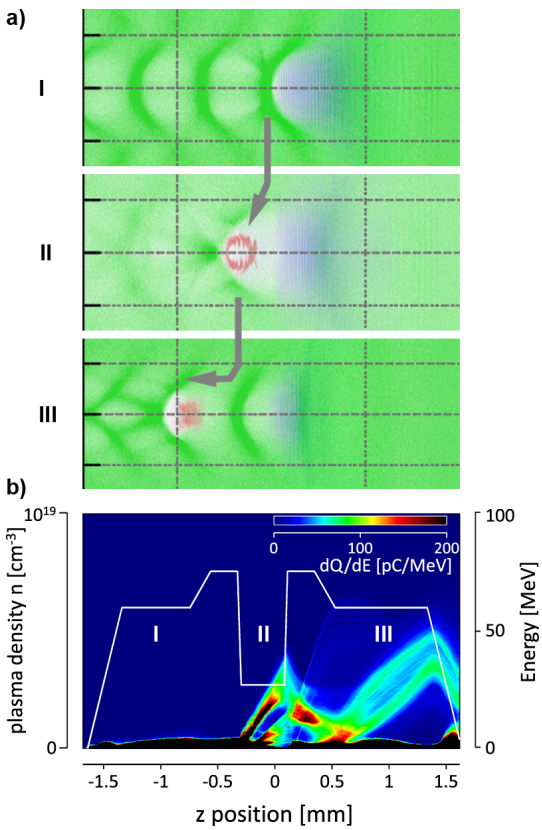

FIG. 5: a) Plasma electron density distribution (green), accelerated electron bunch (red) and laser pulse (blue) shown at the axial section for the instant of laser pulse passing the corresponding density regions I-III. b) Electron energy distribution as a function of the laser pulse z-position and plasma density distribution (white curve).

ilar plasma densities, Mach number and void lengths. Generally, a matched wire injection scheme has to be the goal of future attempts utilizing this scheme.

If acceleration takes place in the first bucket, an effect of the laser field acting directly on the accelerating electron bunch can be observed [33]. Thus electron acceleration in the second bucket, isolated from the laser pulse, may as well explain the experimentally observed reduced divergence. Additionally simulations show a filtering effect during the transition from region II to region III, seemingly reducing the transverse spread of the bunch. Note that the number of injected electrons is sensitive to the plasma density gradient [34].

Using a wire to split the interaction into several stages may increase reproducibility. Decoupling of the pulse self-compression phase from the injection allows the laser pulse to reach a steady state independent of spot fluctuations at the entrance of the gas jet.

In conclusion, the wire injection scheme has successfully been demonstrated as an alternative to more complex two beam setups. Beam features include a by $\approx 25\,\%$ reduced divergence and one order of magnitude charge increase if compared to the nonlinear self-injection case. Their spectra are quasi-monoenergetic features with $\lesssim 1\,\%$ relative spread. For enhanced performance, a matched wire injection regime is proposed, omitting the initial deceleration in the second high density region by adjusting the prevailing density ratios.

We acknowledge the Swedish Research Council, the Knut and Alice Wallenberg Foundation, the Lund University X-Ray Centre, the European Research Council contract number 204059-QPQV, the Swedish Research Council contract number 2010-3727 and the Swedish National Infrastructure for Computing.

[1] T. Tajima *et al.*, Phys. Rev. Lett. **43**, 267 (1979).
[2] S. Backus *et al.*, Rev. Sci. Instrum. **69**, 1207 (1998).
[3] C. G. R. Geddes *et al.*, Nature **431**, 538 (2004).
[4] J. Faure *et al.*, Nature **431**, 541 (2004).
[5] S. P. D. Mangles *et al.*, Nature **431**, 535 (2004).
[6] K. Nakajima *et al.*, Nature Phys. **4**, 92 (200).
[7] H.-P. Schlenvoigt *et al.*, Nature Phys. **4**, 130 (2008).
[8] M. Fuchs *et al.*, Nature Phys. **5**, 826 (2009).
[9] M. Tzoufras *et al.*, Phys. Rev. Lett. **101**, 145002 (2008).
[10] C. Rechatin *et al.*, Phys. Rev. Lett. **103**, 194804 (2009).
[11] C. Rechatin *et al.*, Phys. Rev. Lett. **102**, 164801 (2009).
[12] I. Kostyukov *et al.*, Phys. Rev. Lett. **103**, 175003 (2009).
[13] S. V. Bulanov *et al.*, Phys. Rev. Lett. **78**, 4205 (1997).
[14] A. Zhidkov *et al.*, Physics of Plasmas **11**, 5379 (2004).
[15] E. Esarey *et al.*, Phys. Rev. Lett. **79**, 2682 (1997).
[16] V. Malka *et al.*, Physics of Plasmas **16**, 056703 (2009).
[17] A. Beck *et al.*, New Journal of Physics **13**, 093016 (2011).
[18] J. Faure *et al.*, Nature **444**, 737 (2006).
[19] A. Pak *et al.*, Phys. Rev. Lett. **104**, 025003 (2010).
[20] C. McGuffey *et al.*, Phys. Rev. Lett. **104**, 025004 (2010).
[21] S. Bulanov *et al.*, Phys. Rev. E **58**, R5257 (1998).
[22] C. G. R. Geddes *et al.*, Phys. Rev. Lett. **100**, 215004 (2008).
[23] H. Suk *et al.*, Phys. Rev. Lett. **86**, 1011 (2001).
[24] K. Schmid *et al.*, Phys. Rev. STAB **13**, 091301 (2010).
[25] J. Faure *et al.*, Phys. Plasmas **17**, 083107 (2010).
[26] C.-T. Hsieh *et al.*, Phys. Rev. Lett. **96**, 095001 (2006).
[27] D. Philpott *et al.*, *Mechanics of Flight* (Paperback, 2006).
[28] C. Wang *et al.*, Phys. Rev. STAB **15**, 020401 (2012).
[29] Y. Glinec *et al.*, Rev. Sci. Instrum. **77**, 103301 (2006).
[30] A. Buck *et al.*, Rev. Sci. Instrum. **81**, 033301 (2010).
[31] URL `http://www.ipfran.ru/english/structure/lab334/simlight.html`.
[32] R. G. Hemker *et al.*, Phys. Rev. STAB **5**, 041301 (2002).
[33] S. P. D. Mangles *et al.*, Phys. Rev. Lett. **96**, 215001 (2006).
[34] A. A. Soloviev *et al.*, Nucl. Instrum. Meth. A. **653**, 35 (2011).

Paper III

Enhancement of X-Rays Generated by a Guided Laser Wakefield Accelerator inside Capillary Tubes

J. Ju, K. Svensson, A. Döpp, H. E. Ferrari, K. Cassou, O. Neveu, G. Genoud, F. Wojda, M. Burza, A. Persson, O. Lundh, C.-G. Wahlström, and B. Cros.

Accepted for publication in Appl. Phys. Lett.

Enhancement of X-rays generated by a guided laser wakefield accelerator inside capillary tubes

J. Ju,[1] K. Svensson,[2] A. Döpp,[1] H. E. Ferrari,[3] K. Cassou,[1] O. Neveu,[1] G. Genoud,[2] F. Wojda,[2] M. Burza,[2] A. Persson,[2] O. Lundh,[2] C.-G. Wahlström,[2] and B. Cros[1, a)]

[1)] *Laboratoire de Physique des Gaz et des Plasmas, CNRS-Université Paris-Sud 11, 91405, Orsay, France*

[2)] *Department of Physics, Lund University, P.O. Box 118, S-22100 Lund, Sweden*

[3)] *Consejo Nacional de investigaciones científicas y técnicas (CONICET), Argentina*

Electrons accelerated in the nonlinear regime in a laser wakefield accelerator experience transverse oscillations inside the plasma cavity, giving rise to ultra-short pulsed X-rays, also called betatron radiation. We show that the fluence of X-ray can be enhanced by more than one order of magnitude when the laser is guided by a 10 mm long capillary tube instead of interacting with a 2 mm gas jet. X-rays with a synchrotron-like spectrum and associated critical energy ~ 5 keV, with a peak brightness of $\sim 1 \times 10^{21}$ ph/s/mm^2/mrad^2/0.1%BW, were achieved by employing 16 TW laser pulses.

Since their discovery X-rays have contributed to many fields of science and the development of new X-ray sources is an active field of research. Ultra-short X-ray pulses[1,2] can be generated in a laser wakefield accelerator (LWFA). In the so-called blow-out regime of LWFAs, the ponderomotive force of an intense laser pulse focused in a plasma blows the electrons out of a volume of radius similar to the laser focal spot radius. The charge separation between electrons and ions is associated to electric fields with an amplitude of the order of $\sim$100 GV/m. These fields can trap and accelerate longitudinally plasma electrons to high energy, typically hundreds of MeV, over only a few millimetres, and at the same time wiggle the electrons transversely. The X-ray pulses produced by this mechanism have spectra similar to synchrotron radiation and are often called betatron radiation. The betatron radiation has intrinsically striking features for ultra-fast imaging: a pulse duration on the femtosecond scale[3] and a perfect synchronization to the pump laser.

The use of such X-rays sources for imaging applications has already been demonstrated[4,5] with photon energies in the range 1-10 keV and peak brightness of 10^{22} ph/s/mm^2/mrad^2/0.1%BW. As they are produced by relatively compact laser systems, they have a large potential for dissemination among various user communities. Their development has thus attracted a lot of attention in the past few years, mostly to characterize their properties[3,6,7], or to control them[8,9]. Scalings developed for betatron radiation predict that the X-ray photon energy and brightness can be enhanced by increasing the laser intensity or/and decreasing the plasma density[10]. For example, X-rays extending to 50 keV were observed[11]by using a peak focused intensity larger than 10^{20} W/cm^2. The use of laser guiding in capillary tubes has been shown to enable electron acceleration and X-ray emission at low plasma density and low laser intensity[12,13].

In this letter, we report on the ability to increase the number of photons produced in the 2-10 keV range by using a lower density, longer plasma inside capillary tubes, compared to the plasma density and length usually achieved with gas jets. Using 16 TW laser pulses, the generated X-ray peak brightness is multiplied by 30 when the laser beam is guided by a 10 mm long capillary tube instead of using a 2 mm long gas jet.

Experiments were performed at the Lund Laser Centre, Sweden, where a Ti:Sa, 800 nm central wavelength, laser system delivers an energy of up to 1 J in 40 fs full width at half maximum (FWHM) pulses. A deformable mirror is used after compression to compensate for wavefront distortions in the focal plane. The laser beam was focused, using a $f/15$ off-axis parabola, to an Airy-like spot with 19.7$\pm$0.8 μm radius at first minimum. With an energy of 650 mJ in the focal plane, the peak intensity was estimated to be $(5.4 \pm 0.1)\times10^{18}$ W/cm^2, giving a normalized laser strength parameter $a_0 = 1.6$. Capillary tubes filled with hydrogen gas were used to confine the gas and to partially guide the laser beam. The spectra of electrons accelerated in either a gas jet or capillary tubes were measured by a spectrometer, composed of a 10 cm long permanent magnet, with a central magnetic field of 0.7 T, deflecting the electrons subsequently intercepted by a phosphor screen (Kodak Lanex Regular) imaged onto a CCD camera. Electrons below 42 MeV did not reach the phosphor screen and were not detected. The beam charge was obtained by the absolute calibration of the Lanex screen[14]. X-rays generated by betatron oscillations in the LWFAs were recorded by a X-ray CCD camera placed 110 cm away from the capillary exit on the laser axis, providing a collection angle of 12$\times$12 mrad^2. The X-ray camera was located outside the vacuum chamber, behind a 300 μm thick beryllium window, and a 5 mm air gap. A set of metallic filters (V, Fe, Ni, Sn, and Zr), held together by a 30 μm wire grid, was used in front of the camera to determine the critical energy associated to the X-ray spectrum in the range 2-10 keV.

Fig. 1 shows the main characteristics of the electrons and X-rays produced inside a 10 mm long, 178 μm diameter capillary tube for two values of the plasma electron density, n_e. The electron energy spectra in (b) and (e)

[a)] Electronic mail: brigitte.cros@u-psud.fr

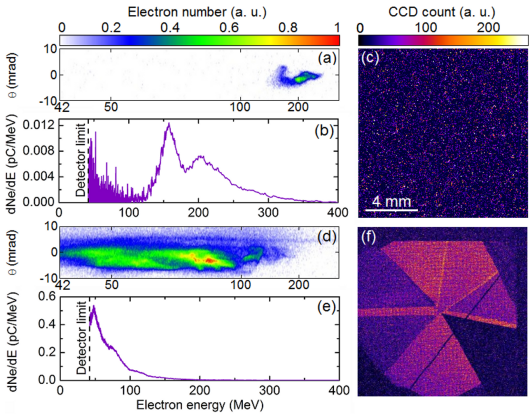

FIG. 1. Single shot raw Lanex images, energy spectra, and X-ray beam images obtained after a 10 mm long, 178 μm diameter capillary tube for two values of the plasma electron density (a) to (c): $n_e = (5.4 \pm 0.3) \times 10^{18}$ cm^{-3}; (d) to (f): $n_e = (8.1 \pm 0.5) \times 10^{18}$ cm^{-3}.

were extracted from the raw Lanex images seen in (a) and (d), respectively, by summing in the vertical direction and rescaling in the horizontal direction to account for magnet dispersion. The electron spectra typically exhibit rather large energy spread and the total charge and maximum energy are strongly dependent on the plasma electron density. The lower density case is close to the density injection threshold[13] and leads to a maximum energy of the order of 300 MeV (measured at 10% of the maximum of the spectrum), with a low beam charge of 0.9 pC, and a divergence FWHM of 5.2 mrad. No X-rays were detected for this shot as seen in Fig. 1(c). At $n_e = (8.1 \pm 0.5) \times 10^{18}$ cm^{-3}, a 18 pC electron bunch was measured with a maximum energy of ∼120 MeV, as shown in Fig. 1(e). The corresponding beam divergence is about 5.8 mrad. Fig. 1(f) shows the associated X-ray beam transmitted through the different filters.

The X-ray spectrum can be characterized by a synchrotron-like[2] spectrum of the form $d^2I/(dEd\Omega)_{\theta=0} \propto (E/E_c)^2\mathcal{K}^2_{2/3}(E/E_c)$, where $\mathcal{K}_{2/3}$ is the modified bessel function of order 2/3. The critical energy is given by $E_c = 3\hbar K\gamma^2\omega_\beta$, where $K = \gamma r_\beta \omega_\beta/c$ is the wiggler strength parameter with γ, r_β, ω_β denoting the relativistic factor, the amplitude and frequency of betatron oscillation, respectively. The critical energy was evaluated from the transmission of X-rays through the different metal filters with a least squares method[11]. In the case of Fig. 1(f), it was found to be 5.4 keV, which is higher than in previous observations[1,12] with similar laser power.

The maximum X-ray fluence measured is $(5.7 \pm 0.6) \times 10^5$ ph/mrad^2 [Fig. 1(f)]. To estimate the peak brightness of this X-ray source, the source size and duration are needed. The source size can be estimated from the expression of critical energy[15] as $r_\beta = E_c c/3\hbar\gamma^3\omega_\beta^2$. The relativistic factor is determined using the mean energy of the electron spectra $\bar{E}_e$, where $\bar{E}_e$ is the average of electron energies weighted by their respective spectral intensities. For the shot plotted in Fig. 1(e), $\bar{E}_e$ is calculated to be 88±4 MeV, and the source size estimated to be $r_\beta = 2 \pm 0.3$ μm. This estimation is validated by 3D simulations performed with the particle-in-cell code CALDER-CIRC[16], for input parameters close to the experimental ones. They show that the laser pulse non linear evolution in the 178 μm diameter capillary tube leads to a maximum normalized vector potential in the range $4 < a_0 < 5.5$, and produces accelerated electrons with a mean energy of about 130 MeV. The transverse and longitudinal sizes of the electron bunch in the simulation are 1.3 μm and 10 μm (∼35 fs), respectively, in reasonable agreement with the estimation from the measurements. The peak brightness achieved in our experiment is estimated, using $r_\beta = 2$ μm, to be $\sim 1 \times 10^{21}$ ph/s/mm^2/mrad^2/0.1%BW, and the wiggler strength parameter, $K \simeq 10$. Taking into account the divergence of the X-ray beam, $\theta = K/\gamma$, the estimated total photon number over the whole spectrum is of the order of 10^9 per shot.

The X-ray fluence can be changed by varying the plasma density, as presented in Fig. 2 for two different capillaries. In both cases, the X-ray fluence is maximum

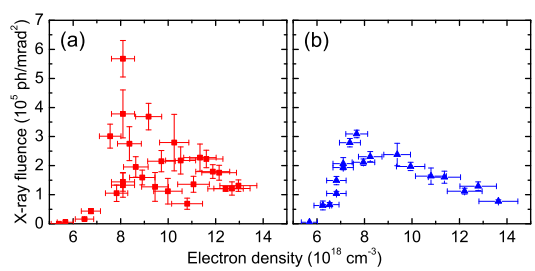

FIG. 2. X-ray fluence as a function of the plasma electron density for (a) a 10 mm long, 178 μm diameter capillary and (b) a 20 mm long, 152 μm diameter capillary; the other parameters are the same as for Fig. 1.

for a density of the order of 8×10^{18} cm^{-3}. The influence of the plasma electron density on the X-ray fluence can be understood as a result of the influence of the density on the laser propagation and related electron injection and acceleration. For the parameters of this experiment, at lower densities, electron trapping is not efficient, resulting in a lower beam charge, as seen in Fig. 1. As the plasma density is increased, trapping becomes more efficient and more charge can be accelerated but the acceleration length and thus the electron energy, become smaller due to the shortening of the electron dephasing and laser depletion lengths. For the given laser intensity, the maximum X-ray fluence is achieved in the 10 mm long capillary tube. Simulations in the 178 μm capillary tube

for the optimum electron density show that the overall process of laser non-linear evolution, electron injection and acceleration, and X-ray emission occur over the first 10 mm of propagation. Fluctuations of the X-ray fluence are smaller at the output of the 152 μm diameter, 20 mm long capillary: this can be attributed to the fact that the capillary diameter is smaller favoring a more stable laser guiding. In this case more X-rays are produced at low densities: it can be due to higher intensities achieved locally inside the capillary, or an evolution of the laser pulse leading to electron injection and acceleration over a distance larger than 10 mm.

The enhancement of the X-ray fluence due to the length and density of the plasma is demonstrated in Fig. 3 by the comparison of the X-ray fluence measured for two targets, 10 mm long capillary tube and 2 mm gas jet, for the same experimental conditions. It shows that for

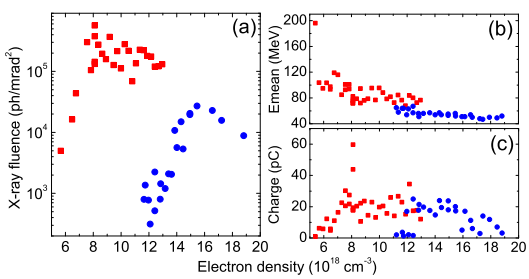

FIG. 3. (a) X-ray fluence, (b) mean energy and (c) charge of electrons as a function of plasma density for the 10 mm long capillary (red squares) and the 2 mm gas jet (blue dots).

the intensity used in this experiment, the use of a capillary tube allows electron self-injection to happen at lower density than in the gas jet. The capillary provides a long distance for laser evolution to the threshold required for self-trapping[12,13], and helps collecting and refocusing the energy initially in the wings of the laser spot[16]; the excitation of multiple modes and their beating can also give rise locally to higher intensity than in vacuum, thus favoring an increase of a_0. For the gas jet, electron trapping starts around $n_e = 11 \times 10^{18}$ cm^{-3}, which results in lower energy electrons, as electron energy inversely depends on plasma density. In the intermediate density range $(11 - 13) \times 10^{18}$ cm^{-3}, a higher mean electron energy is achieved when the capillary is employed. The maximum X-ray fluence in the capillary corresponds to the density where the maximum electron charge is measured. The maximum X-ray fluence obtained with the gas jet is 2.7×10^4 ph/mrad^2 for $n_e = 15 \times 10^{18}$ cm^{-3}. Using the values obtained from experimental data, $E_c = 4.6$ keV, $\bar{E}_e = 56$ MeV, the source size is estimated to be 2.4 μm and the corresponding peak brightness is $\sim 3 \times 10^{19}$ ph/s/mm^2/mrad^2/0.1%BW, similar to the result of Ref. [1].

In conclusion, we demonstrate that betatron radiation is significantly enhanced by guiding the laser in a capillary tube allowing electron acceleration in a low density, long plasma. In particular, $\sim 1 \times 10^{21}$ ph/s/mm^2/mrad^2/0.1%BW is the brightest X-ray beam achieved with a <20 TW laser. The dependence of the X-ray beam parameters on the capillary tube diameter and length provide additional control of the interaction and its systematic study will be the subject of future work.

This work was supported by LASERLAB-EUROPE (grant agreement 228334), the Triangle de la Physique (grant agreement NEXT-2009-064T), the Lund University X-ray Center (LUXC), the Swedish Research Council (including the Linné grant to LLC), and the Knut and Alice Wallenberg Foundation. J. Ju acknowledges financial support from the Chinese Scholarship Council.

[1] A. Rousse, K. Ta Phuoc, R. Shah, A. Pukhov, E. Lefebvre, V. Malka, S. Kiselev, F. Burgy, J.-P. Rousseau, D. Umstadter, and D. Hulin, Phys. Rev. Lett. **93**, 135005 (2004).

[2] E. Esarey, B. A. Shadwick, P. Catravas, and W. P. Leemans, Phys. Rev. E **65**, 056505 (2002).

[3] K. Ta phuoc, R. Fitour, A. Tafzi, T. Garl, N. Artemiev, R. Shah, F. Albert, D. Boschetto, A. Rousse, D-E. Kim, A. Pukhov, V. Seredov, I. Kostyukov, Phys. Plasmas **14**, 080701 (2007).

[4] S. Kneip, C. McGuffey, F. Dollar, M. S. Bloom, V. Chvykov, G. Kalintchenlko, K. Krushelnick, A. Maksimchuk, S. P. D. Mangles, T. Matsuoka, Z. Najmudin, C. A. J. Palmer, J. Schreiber, W. Schumaker, A. G. R. Thomas, and V. Yanovsky, Appl. Phys. Lett. **99**, 093701 (2011).

[5] S. Fourmaux, S. Corde, K. Ta Phuoc, P. Lassonde, G. Lebrun, S. Payeur, F. Martin, S. Sebban, V. Malka, A. Rousse, and J. C. Kieffer, Opt. Lett. **36**, 2426 (2011).

[6] R. C. Shah, F. Albert, K. Ta Phuoc, O. Shevchenko, D. Boschetto, A. Pukhov, S. kiselev, F. Burgy, J.-P. Rousseau, and A. Rousse, Phys. Rev. E **74**, 045401(R) (2006).

[7] S. Fourmaux, S. Corde, K. Ta Phuoc, P. M. Leguay, S. Payeur, P. Lassonde, S. Gnedyuk, G. Lebrun, C. Fourment, V. Malka, S. Sebban, A. Rousse and J. C. Kieffer, New J. Phys. **13**, 033017 (2011).

[8] S. P. D. Mangles, G. Genoud, S. Kneip, M. Burza, K. Cassou, B. Cros, N. P. Dover, C. Kamperidis, Z. Najmudin, A. Persson, J. Schreiber, F. Wojda, and C.-G. Wahlström, Appl. Phys. Lett. **95**, 181106 (2009).

[9] K. Ta Phuoc, E. Esarey, V. Leurent, E. Cormier-Michel, C. G. R. Geddes, C. B. Schroeder, A. Rousse, and W. P. Leemans, Phys. Plasmas **15**, 063102 (2008).

[10] A. G. R. Thomas, Phys. Plasmas **17**, 056708 (2010).

[11] S. Kneip, S. R. Nagel, C. Bellei, N. Bourgeois, A. E. Dangor, A. Gopal, R. Heathcote, S. P. D. Mangles, J. R. Marquès, A. Maksimchuk, P. M. Nilson, K. Ta Phuoc, S. Reed, M. Tzoufras, F. S. Tsung, L. Willingale, W. B. Mori, A. Rousse, K. Krushelnick, and Z. Najmudin, Phys. Rev. Lett. **100**, 105006 (2008).

[12] G. Genoud, K. Cassou, F. Wojda, H. E. Ferrari, C. Kamperidis, M. Burza, A. Persson, J. Uhlig, S. Kneip, S. P. D. Mangles, A. Lifschitz, B. Cros, and C.-G. Wahlström, Appl. Phys. B **105**, 309 (2011).

[13] H. E. Ferrari, A. F. Lifschitz, G. Maynard, and B. Cros, Phys. Plasmas **18**, 083108 (2011).

[14] Y. Glinec, J. Faure, A. Guemnie-Tafo, V. Malka, H. Monard, J. P. Larbre, V. De Waele, J. L. Marignier, and M. Mostafavi, Rev. Sci. Instrum. **77**, 103301 (2006).

[15] F. Albert, R. Shah, K. Ta Phuoc, R. Fitour, F. Burgy, J.-P. Rousseau, A. Tafzi, D. Douillet, T. Lefrou, and A. Rousse, Phys. Rev. E **77**, 056402 (2008).

[16] H. E. Ferrari, A. Lifschitz, and B. Cros, Plas. Phys. Contr. Fus. **53**, 014005 (2011).

Paper IV

Self-Injection Threshold in Self-Guided Laser Wakefield Accelerators

S. P. D. Mangles, G. Genoud, M. S. Bloom, M. Burza, Z. Najmudin, A. Persson, K. Svensson, A. G. R. Thomas and C.-G. Wahlström.

Phys. Rev. ST Accel. Beams **15**, 011302 (2012).

PHYSICAL REVIEW SPECIAL TOPICS - ACCELERATORS AND BEAMS **15**, 011302 (2012)

Self-injection threshold in self-guided laser wakefield accelerators

S. P. D. Mangles,[1] G. Genoud,[2] M. S. Bloom,[1] M. Burza,[2] Z. Najmudin,[1]
A. Persson,[2] K. Svensson,[2] A. G. R. Thomas,[3] and C.-G. Wahlström[2]

[1]*The Blackett Laboratory, Imperial College London, SW7 2AZ, United Kingdom*
[2]*Department of Physics, Lund University, P.O. Box 118, S-22100 Lund, Sweden*
[3]*Center for Ultrafast Optical Science, University of Michigan, Ann Arbor, Michigan 48109, USA*

(Received 7 January 2011; published 19 January 2012)

A laser pulse traveling through a plasma can excite large amplitude plasma waves that can be used to accelerate relativistic electron beams in a very short distance—a technique called laser wakefield acceleration. Many wakefield acceleration experiments rely on the process of wave breaking, or self-injection, to inject electrons into the wave, while other injection techniques rely on operation without self-injection. We present an experimental study into the parameters, including the pulse energy, focal spot quality, and pulse power, that determine whether or not a wakefield accelerator will self-inject. By taking into account the processes of self-focusing and pulse compression we are able to extend a previously described theoretical model, where the minimum bubble size $k_p r_b$ required for trapping is not constant but varies slowly with density and find excellent agreement with this model.

DOI: 10.1103/PhysRevSTAB.15.011302 PACS numbers: 52.38.Kd, 41.75.Jv, 52.35.Mw

Laser wakefield acceleration, where an intense laser pulse drives a plasma wave with a relativistic phase velocity, is a promising technique for the development of compact, or ''tabletop,'' particle accelerators and radiation sources. Plasma waves driven in moderate density plasmas can support electric fields over a thousand times stronger than those in conventional accelerators. Laser driven plasma waves have demonstrated electron acceleration to $\simeq 1$ GeV in distances $\simeq 1$ cm [1–3]. These compact particle accelerators have significant potential as bright x-ray sources [4–6] offering peak brightness comparable to 3rd generation synchrotron sources in x-ray flashes on the order of just 10 fs.

At the heart of the laser wakefield acceleration concept is the fact that electron plasma waves with relativistic phase velocities are driven to very large amplitudes, where they become highly nonlinear. If the plasma wave is driven beyond a threshold amplitude, the wave breaks. When the wave is driven far beyond the wave breaking threshold, the wave structure is destroyed and large amounts of charge can be accelerated to high energy but with a broad energy spread [7]. With appropriately shaped laser pulses this normally catastrophic process of wave breaking can be tamed to produce high quality beams of electrons. This is because close to the wave breaking threshold the nature of wave breaking changes—some electrons from the background plasma can become trapped in the wave without destroying the wave structure, a process called self-injection.

The highly nonlinear broken wave regime [8] is used in many experiments to produce quasimonoenergetic electron beams [9–11]. In such experiments a threshold plasma density is commonly observed, below which no electron beams are produced. Because of the inverse scaling of the electron beam energy with plasma density, the highest energy beams achievable with a given laser system are achieved just above the threshold, and it is well known that many of the beam parameters including the spectrum and stability are also optimized just above the threshold density [12,13]. It is also well known that to achieve self-injection at lower densities higher power lasers are required—although the exact scaling of the threshold with laser power is not well known. A number of techniques to improve the electron beam parameters including stability and total charge have recently been demonstrated by using alternative injection schemes [14–18]. Crucially these schemes all rely on operating the laser wakefield accelerator (LWFA) below the self-injection threshold. A number of recent purely theoretical papers have addressed the dynamics of wave breaking or self-injection [19–22]. Clearly a good understanding of the self-injection threshold is important for the development of laser wakefield accelerators. We report here on a series of experiments which identify the key laser and plasma parameters needed to predict the density threshold and we develop a model capable of predicting the self-injection threshold density for a given set of experimental parameters.

In LWFA experiments the laser pulse self-focuses due to the transverse nonlinear refractive index gradient of the plasma [23,24] and the spot size decreases towards a matched spot size. This matched spot size occurs when the ponderomotive force of the laser balances the space charge force of the plasma bubble formed. In situations

Published by the American Physical Society under the terms of the Creative Commons Attribution 3.0 License. Further distribution of this work must maintain attribution to the author(s) and the published article's title, journal citation, and DOI.

where there is no loss of energy during self-focusing, nor any change in the pulse duration, the final matched spot size, and hence the final intensity, is simply a function of $\alpha P/P_c$. P is the laser power; α is the fraction of laser energy within the full width at half maximum intensity of the focal spot—important because energy in the wings of the spot are not self-focused by the plasma wave and so do not contribute; P_c is the laser power where relativistic self-focusing dominates over diffraction, $P_c = (8\pi\epsilon_0 m_e^2 c^5/e^2)(n_c/n_e) \simeq 17 n_c/n_e$ GW (where n_e is the background plasma electron density and n_c is the critical density for propagation of the laser in the plasma). We might therefore expect that the self-injection threshold would occur at a fixed value of $\alpha P/P_c$ [25]. However, it is also known that the longitudinal nonlinear refractive index gradient also has a significant effect on the pulse properties [26,27] and we expect this to have an affect on the self-injection threshold.

The experiment was carried out using the multi-TW laser at the Lund Laser Centre. The laser delivered pulse energies of up to 0.7 J in pulses as short as 40 fs, corresponding to a peak power of 18 TW. An f/9 off-axis parabolic mirror was used to focus the pulse. A deformable mirror was used to optimize the focal spot, producing a spot size of 16 ± 1 μm FWHM. For a Gaussian focal spot the theoretical maximum fraction of energy within the FWHM is $\alpha = 1/2$, the best focus that we obtained had $\alpha = 0.48$. The focal plane was positioned onto the front edge of a supersonic helium gas jet with an approximately flat top profile of length 1.8 ± 0.1 mm.

To investigate the self-injection threshold, we studied the effect of the plasma density n_e, the total laser energy E, the focal spot quality α, and the pulse duration τ on the amount of charge in the electron beam. We chose to use the total charge in the electron beam as the diagnostic of self-injection as it provides a clear unambiguous signal of an electron beam.

The charge was measured using an electron beam profile monitor, consisting of a Lanex screen placed on the back surface of a wedge (which was used to collect the transmitted laser light). The wedge was 1 cm thick and made of glass and therefore prevented electrons below approximately 4 MeV reaching the Lanex. The Lanex screen was imaged onto a 12 bit CCD camera. To reduce the amount of background light from the interaction, a narrow band interference filter matched to the peak emission of the Lanex screen was placed in front of the camera. In addition, the camera was triggered several microseconds after the interaction but within the lifetime of the Lanex fluorescence. The Lanex screen was calibrated using the absolute efficiency data, absolute response of the CCD camera, and the details of the imaging system [28]. A beam profile monitor was used in preference to an electron spectrometer due to the fact that it has a higher sensitivity (i.e. the signal produced by a low charge beam dispersed inside a spectrometer will drop below the background level, whereas the same low charge beam will produce a bright image on the profile monitor). Also close to the threshold we do not expect the electrons to have particularly high energy (i.e. injection could be occurring but the electron beam energy could be outside the range of the electron spectrometer).

The gas jet could produce electron densities up to $n_e = 5 \times 10^{19}$ cm^{-3}. The laser pulse energy was varied by altering the energy pumping the final laser amplifier. We used the deformable mirror to reduce α by adding varying amounts of spherical aberration. Spherical aberration has the effect of decreasing α without introducing asymmetry to the focal spot and without significantly affecting its size. Degrading the focal spot symmetrically was desirable as asymmetric pulses can drive asymmetric wakes which can have a strong effect on the dynamics of self-injection [29]. The pulse duration was altered by changing the separation of the gratings in the compressor. Changing the grating separation introduced both a chirp to the pulse spectrum and a skew to the pulse envelope. To take this into account, we investigated both positive and negative chirps.

Figure 1 shows the effect of varying the laser pulse energy within the focal spot on the self-injection threshold. Keeping the total laser energy constant and degrading the focal spot (i.e. lowering α) moves the threshold to higher plasma densities. We also observe an increase in the threshold density when we keep α constant and reduce the laser pulse energy. In fact, we find that the two effects are equivalent, i.e., that the threshold shifts according to the product αE. This demonstrates that it is only the energy within the FWHM of the focal spot that contributes to driving the plasma wave. This emphasizes the importance

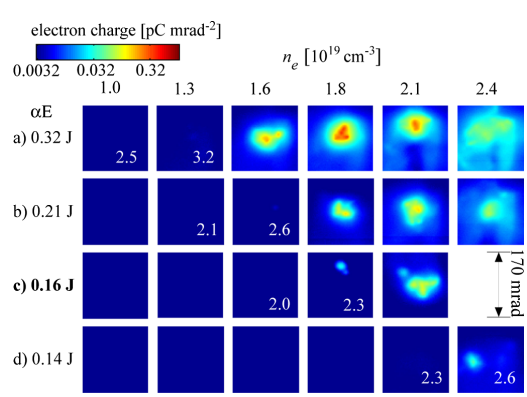

FIG. 1. Electron beam profiles for various plasma densities for different values of the amount of laser energy within the FWHM of the focal spot. (a), (b), and (d) kept the total laser energy constant but varied α whereas (c) reduced the laser energy. Each panel is an average of five shots and is displayed on a logarithmic color scale.

of laser focal spot quality in LWFA experiments [30], which are often performed with $\alpha \approx 0.3$ [2,25]. Improving the focal spot could therefore result in a significant increase in the electron beam energy achievable from a given laser system.

The observed variation of the threshold with αE is as expected for one based on $\alpha P/P_c$ but this can only be confirmed by the behavior of the threshold when we vary the laser pulse duration, keeping αE constant. When we do this we see markedly different behavior.

We kept the plasma density constant, at a value just above the threshold density for the optimally compressed pulse. At this density ($n_e = 1.6 \times 10^{19}$ cm^{-3}), with full laser energy ($\alpha E = 0.32$ J) and the fully compressed pulse ($\tau = 42$ fs) we observed a bright electron beam. When we reduced either the plasma density or the pulse energy by a small factor (20%–25%) this beam disappeared, i.e., we dropped below the threshold. Even after increasing the pulse duration by a factor of 2, electrons are clearly still injected, as shown in Fig. 2. This is true regardless of the chirp of the laser pulse, however we do see an enhancement of the total charge using positively chirped (red at the front) pulses as reported previously [31]. These pulses have a fast rising edge indicating that the precise shape of the pulse may play a role in the total charge injected. The direction of chirp of the pulse may also affect the rate at which pulse compression occurs [32]. For both directions of chirp the fact that the threshold behavior is so significantly different to that observed when varying αE suggests that pulse compression is indeed playing an important role in determining whether or not the accelerator reaches wave breaking.

In Fig. 3 we plot the total charge observed on the profile monitor screen for the various data sets. Figure 3(a) shows the total charge, plotted against the pulse power normalized to the critical power for self-focusing, for the data sets where we varied the plasma density and the energy within the focal spot (either by varying the spot quality α or total pulse energy E). The charge rises rapidly with increasing $\alpha P/P_c$ until eventually reaching a plateau at

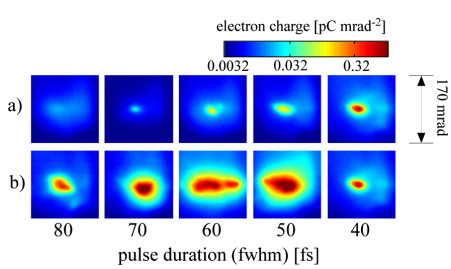

FIG. 2. Electron beam profiles for various pulse durations at fixed αE and at a plasma density just above the threshold density for injection for 40 fs pulses. The pulse duration was varied by changing the compressor grating separation which introduces a chirp to the pulse: (a) negative chirp; (b) positive chirp.

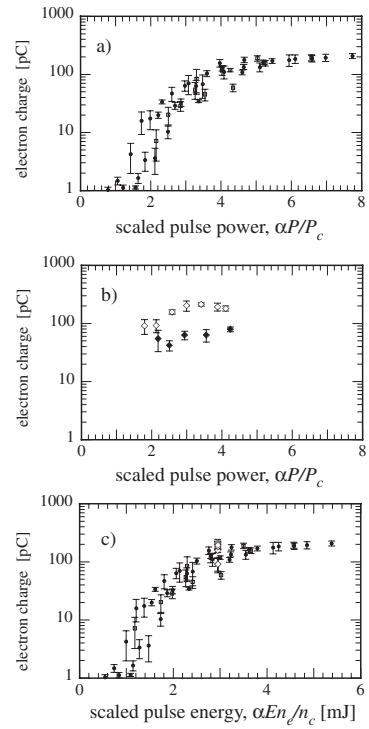

FIG. 3. (a) Electron charge (>4 MeV) versus $\alpha P/P_c$ keeping the pulse duration constant but varying focal spot quality and plasma density (closed circles) or total pulse energy and plasma density (open squares) but keeping pulse duration constant. (b) Electron charge versus $\alpha P/P_c$ varying pulse duration while keeping plasma density and energy in focal spot constant. (c) Data from (a) and (b) plotted versus $\alpha E n_e/n_c$. Each data point is an average of five shots and the error bars represent 1 standard deviation.

around $\alpha P/P_c \approx 4$. There is an increase in the total charge of a factor of 10 between $\alpha P/P_c = 2$ and $\alpha P/P_c = 4$ for both sets of data. The fact that both data sets lie on the same curve confirms the fact that it is the energy within the focal spot which determines the wakefield behavior. This supports the hypothesis that energy in the wings of the focal spot is not coupled into the accelerator: energy in the wings of the spot is effectively wasted.

Figure 3(b) shows the charge plotted against $\alpha P/P_c$ for a data set where we kept the plasma density and αE constant but varied the pulse duration (by introducing either positive or negative chirp). The markedly different behavior is once again apparent: rather than the rapid increase of charge between $\alpha P/P_c = 2$ and $\alpha P/P_c = 4$ the charge is approximately constant for each data set.

Figure 3(c) plots all of the data sets (varying α, E, and τ) against a scaled pulse energy $\alpha E n_e/n_c$ rather than the

scaled pulse power. The fact that the pulse duration data set now fits closely with the αE data sets confirms that pulse compression is playing an important role in determining whether or not the wakefield accelerator reaches self-injection.

A recent paper that examined the trajectory of electrons inside the plasma bubble [21] predicts that self-trapping will occur when the radius of the plasma bubble (r_b) is larger than a certain value given by

$$k_p r_b > 2\sqrt{\ln(2\gamma_p^2) - 1}, \tag{1}$$

where $\gamma_p \approx \sqrt{n_c/(3n_e)}$ [33] is the Lorentz factor associated with the phase velocity of the bubble. When this condition is met, an electron starting at rest a distance r_b from the laser axis and following an elliptical trajectory in the bubble fields (thus defining the edge of the bubble) will be accelerated by the bubble fields up to $\gamma_p m_e c^2$ by the time it reaches the back of the bubble. A key feature of this model is that the normalized bubble size required for self-injection $k_p r_b$ is not constant with density. As Eq. (1) depends only on the plasma density and bubble size, we can determine the minimum pulse properties required to reach the threshold by noting that the radius of the bubble is related to the pulse energy and duration through [34]

$$k_p r_b = 2\sqrt{2}\left(\frac{\alpha E}{\tau P_c}\right)^{1/6}. \tag{2}$$

Combining Eqs. (1) and (2) yields an expression for the minimum pulse energy required to reach self-injection:

$$\alpha E > \frac{\pi \epsilon_0 m_e^2 c^5}{e^2}\left[\ln\left(\frac{2n_c}{3n_e}\right) - 1\right]^3 \frac{n_c}{n_e}\tau(l), \tag{3}$$

where $\tau(l)$ is the pulse duration after a propagation length l. A simple model for the rate of pulse compression was put forward in Ref. [27] based on the fact that the front of the pulse travels at the group velocity of the laser in the plasma and the back of the pulse travels in vacuum, this produces $\tau(l) \approx \tau_0 - (n_e l)/(2cn_c)$. The interaction length will be limited by either the length of the plasma target or the pump depletion length $l_{\rm pd} \simeq c\tau_0 n_c/n_e$ [34]. For the depletion limited case Eq. (3) reduces to

$$\frac{\alpha P}{P_c} > \frac{1}{16}\left[\ln\left(\frac{2n_c}{3n_e}\right) - 1\right]^3. \tag{4}$$

The threshold density for self-injection for a given experiment can be calculated from (3) and (4). This model requires knowledge of the initial pulse energy, pulse duration, and the length of the plasma to predict the threshold. As Eqs. (3) and (4) are transcendental, the density threshold for a given laser system must be found numerically.

A previous study showed that, at low density, the threshold is approximately $\alpha P/P_c > 3$ [25], this can be rearranged into a similar form to Eq. (3):

$$\alpha E > 3\frac{\pi \epsilon_0 m_e^2 c^5}{e^2}\frac{n_c}{n_e}\tau_0. \tag{5}$$

We can then use Eq. (5) to predict the density threshold for specific experimental conditions. To use this model only the initial pulse power is required to calculate the threshold density. Combining $\alpha P/P_c > 3$ and Eq. (2) reveals that this threshold model is also equivalent to stating that the minimum bubble size for self-trapping is constant with density ($k_p r_b > 3.4$) in contrast to Eq. (1).

In Fig. 4 we plot the variation of the observed threshold density with laser energy (αE). We have defined the experimentally observed threshold density as lying in the region between the highest density where we observe no electron beam and the lowest density where we clearly observe a beam. We also show the theoretical threshold density based on Eqs. (3) and (4), and the predicted threshold based on Eq. (5). Its agreement with the experimental data indicates that our model accurately predicts the self-injection threshold, confirming that the threshold is reached because the laser pulse undergoes intensity amplification due to a combination of pulse compression and self-focusing.

Our measurements of the threshold density for self-injection have been made with only moderate laser pulse energies ~1 J. Many laser wakefield experiments are now being performed with pulse energies ~10 J and the validity of this model at these higher laser energies can be verified by applying it to previously published data. We restrict ourselves to data obtained from experiments with gas jets as guiding structures can affect the trapping threshold by changing the way pulse evolution occurs [30] or by introducing additional effects such as ionization injection [35]. To calculate the density threshold for a particular set of experimental parameters, the following information is required: the laser energy E, the focal spot quality α, the initial pulse duration τ, and the maximum plasma length l. Equations (3) and (4) or Eq. (5) can then be used to calculate the expected density threshold for the two models. Kneip *et al.* [2], using a 10 J, 45 fs, 800 nm laser pulse

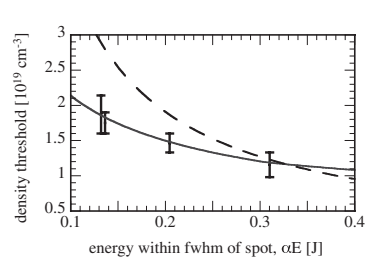

FIG. 4. Observed density threshold as a function of laser energy (αE) for our experiment. The solid curve represents our threshold model. The dashed curve represents a threshold based on $\alpha P/P_c > 3$.

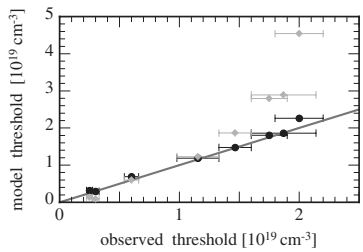

FIG. 5. Plot of reported density threshold, n_t, versus predicted density threshold, n_{model}, for this and other published experiments [2,11,25,36]. Circles show the predictions of our model, diamonds show the threshold based on $\alpha P/P_c > 3$. The line indicates $n_t = n_{\mathrm{model}}$.

with $\alpha = 0.3$, observed a threshold density of $n_e = 2\text{–}3 \times 10^{18}$ cm^{-3} in an 8.5 mm long plasma; our model predicts that the threshold density for self-injection should occur at $n_e \approx 3 \times 10^{18}$ cm^{-3}. Froula *et al.* [25], using a 60 fs, 800 nm laser with $\alpha E \approx 6$ J, observed a threshold density of $n_e \approx 3 \times 10^{18}$ cm^{-3} in an 8.0 mm plasma; our model also predicts $n_e \approx 3 \times 10^{18}$ cm^{-3}. Schmid *et al.* [36] using an 8 fs, 840 nm laser with $\alpha E \approx 15$ mJ, observed electron beams at a density of $n_e \approx 2 \times 10^{19}$ cm^{-3} in a plasma 300 μm long; our model predicts a threshold of $n_e \approx 2.2 \times 10^{19}$ cm^{-3}. Faure *et al.* [11], using a 33 fs, 820 mn laser, reported a dramatic decrease in the number of accelerated electrons at $n_e \approx 6 \times 10^{18}$ cm^{-3} in a 3 mm gas jet with $\alpha E \approx 0.5$ J. Our model predicts a threshold density of $n_e \approx 7 \times 10^{18}$ cm^{-3}.

These additional data points, together with those from this experiment, are presented in Fig. 5. Because of the fact that our model does not depend on a single experimental parameter, we plot the experimentally observed density threshold n_t for each experiment on the x axis and against the calculated threshold n_{model} obtained using either Eqs. (3) and (4) or Eq. (5). Figure 5 shows that our model is in good agreement with experiments over nearly 3 orders of magnitude in laser energy, whereas the threshold based on Eq. (5) matches the observed threshold over only a very limited range of pulse energies: it overestimates the threshold density for low energy laser systems and, on the other hand, would significantly underestimate the threshold for very high energy laser systems.

We note that simulations by Yi *et al.* [22] show that, at very low density and an initial laser spot size less than the matched spot size, diffraction of the laser pulse leads to a lengthening of the bubble which plays a role in determining self-injection. In that work they see self-injection with a 200 J, 150 fs laser pulse at a density of $n_e = 10^{17}$ cm^{-3}. Our model predicts that the threshold would be $n_e \approx 4 \times 10^{17}$ cm^{-3}—actually in reasonable agreement with [22], however our model relies on pulse compression occurring over ≈ 10 cm whereas Yi *et al.* show that in their simulations injection occurs after just 5 mm. This indicates that our model is only valid for initial laser spot sizes *greater than or equal to* the matched spot size (as is the case for the experiments shown in Fig. 5).

We now use our model to predict the self-injection threshold density for lasers currently under construction. For example, our model predicts that a 10 PW laser (300 J in 30 fs, $\lambda = 0.9$ μm, such as the Vulcan 10 PW laser at the Rutherford Appleton Lab, or the ELI Beamlines facility in the Czech Republic) could produce electron injection at as low as $n_e \approx 2 \times 10^{17}$ cm^{-3} (assuming $\alpha = 0.5$) in a 6 cm long plasma. For a 1 PW laser (40 J in 40 fs, $\lambda = 0.8$ μm, such as the Berkley Lab Laser Accelerator, BELLA), our model predicts that self-injection will occur at a density of $n_e \approx 9 \times 10^{17}$ cm^{-3} in 2.4 cm.

The lower the threshold density of a wakefield accelerator, the higher the maximum beam energy. However, for self-injecting accelerators there must be acceleration after injection, requiring operation at densities slightly above this threshold so that injection occurs earlier in the interaction.

In summary, we have measured the effect of various laser parameters on the self-injection threshold in laser wakefield accelerators. The simple model we use relies on the fact that pulse compression and self-focusing occur and that only the energy within the FWHM of the focal spot contributes towards driving the plasma wave. We find that in cases where the interaction is limited by pump depletion, the threshold can be expressed as a ratio of P/P_c, but this ratio is not the same for all laser systems: for higher power lasers the threshold occurs at a higher value of P/P_c than for lower power lasers. When the plasma length is shorter than the pump depletion length, we find that the length of the plasma is an important parameter in determining the injection threshold.

ACKNOWLEDGMENTS

This work was supported by the Royal Society, EPSRC (Grant No. EP/I014462/1); the Swedish Research Council (including the Linné grant to the LLC); the Knut and Alice Wallenberg Foundation; the EU Access to Research Infrastructures activity, FP7 Grant Agreement No 228334: Laserlab Europe, the Lund University X-ray Centre (LUXC); and the Marie Curie Early Stage Training Site MAXLAS (Contract No. MEST-CT-2005-020356).

[1] W. P. Leemans *et al.*, Nature Phys. **2**, 696 (2006).
[2] S. Kneip *et al.*, Phys. Rev. Lett. **103**, 035002 (2009).
[3] C. E. Clayton *et al.*, Phys. Rev. Lett. **105**, 105003 (2010).
[4] A. Rousse *et al.*, Phys. Rev. Lett. **93**, 135005 (2004).
[5] S. Kneip *et al.*, Nature Phys. **6**, 980 (2010).
[6] M. Fuchs *et al.*, Nature Phys. **5**, 826 (2009).
[7] A. Modena *et al.*, Nature (London) **377**, 606 (1995).

[8] A. Pukhov and J. Meyer-ter Vehn, Appl. Phys. B **74**, 355 (2002).
[9] S. P. D. Mangles *et al.*, Nature (London) **431**, 535 (2004).
[10] C. G. R. Geddes *et al.*, Nature (London) **431**, 538 (2004).
[11] J. Faure *et al.*, Nature (London) **431**, 541 (2004).
[12] V. Malka *et al.*, Phys. Plasmas **12**, 056702 (2005).
[13] S. P. D. Mangles *et al.*, Phys. Plasmas **14**, 056702 (2007).
[14] J. Faure *et al.*, Nature (London) **444**, 737 (2006).
[15] C. McGuffey *et al.*, Phys. Rev. Lett. **104**, 025004 (2010).
[16] A. Pak *et al.*, Phys. Rev. Lett. **104**, 025003 (2010).
[17] C. G. R. Geddes *et al.*, Phys. Rev. Lett. **100**, 215004 (2008).
[18] K. Schmid *et al.*, Phys. Rev. ST Accel. Beams **13**, 091301 (2010).
[19] S. Kalmykov *et al.*, Phys. Rev. Lett. **103**, 135004 (2009).
[20] I. Kostyukov *et al.*, Phys. Rev. Lett. **103**, 175003 (2009).
[21] A. G. R. Thomas, Phys. Plasmas **17**, 056708 (2010).
[22] S. A. Yi, V. Khudik, S. Kalmykov, and G. Shvets, Plasma Phys. Controlled Fusion **53**, 014012 (2011).
[23] A. G. R. Thomas *et al.*, Phys. Rev. Lett. **98**, 095004 (2007).
[24] J. E. Ralph *et al.*, Phys. Rev. Lett. **102**, 175003 (2009).
[25] D. H. Froula *et al.*, Phys. Rev. Lett. **103**, 215006 (2009).
[26] J. Faure *et al.*, Phys. Rev. Lett. **95**, 205003 (2005).
[27] J. Schreiber *et al.*, Phys. Rev. Lett. **105**, 235003 (2010).
[28] Y. Glinec *et al.*, Rev. Sci. Instrum. **77**, 103301 (2006).
[29] S. P. D. Mangles *et al.*, Appl. Phys. Lett. **95**, 181106 (2009).
[30] T. P. A. Ibbotson *et al.*, Phys. Rev. ST Accel. Beams **13**, 031301 (2010).
[31] W. P. Leemans *et al.*, Phys. Rev. Lett. **89**, 174802 (2002).
[32] E. S. Dodd and D. Umstadter, Phys. Plasmas **8**, 3531 (2001).
[33] C. D. Decker *et al.*, Phys. Plasmas **3**, 2047 (1996).
[34] W. Lu *et al.*, Phys. Rev. ST Accel. Beams **10**, 061301 (2007).
[35] T. P. Rowlands-Rees *et al.*, Phys. Rev. Lett. **100**, 105005 (2008).
[36] K. Schmid *et al.*, Phys. Rev. Lett. **102**, 124801 (2009).